

Galactic evolution along the Hubble Sequence
I. A grid of models parametrized by initial galaxy mass distribution

Mercedes Mollá, Angeles I. Díaz

Departamento de Física Teórica, Universidad Autónoma de Madrid, 28049 Cantoblanco

mercedes.molla@uam.es

angeles.diaz@uam.es

Federico Ferrini¹

Dipartimento di Fisica, Università di Pisa, Piazza Torricelli 2, 56100 Pisa, Italia

ferrini@intas.be

ABSTRACT

We present a generalization of the multiphase chemical evolution model applied to a wide set of theoretical galaxies with different masses and morphological types. This generalized set of models has been computed using the so-called *Universal Rotation Curve* from Persic, Salucci & Steel (1996) to calculate the radial mass distribution of 44 *theoretical* protogalaxies. This distribution is a fundamental input which, besides its own effect on the galaxy evolution, defines the characteristic collapse time scale or gas infall rate onto the disk.

On the other hand, the molecular cloud and star formation efficiencies take 10 different values between 0 and 1, as corresponding to their probability nature, for each one of the radial distributions of total mass. This implies that for each mass radial distribution, we have 10 different evolutionary rates, which happen to be related to the morphological types of galaxies, as we will later show. With these two hypotheses we construct a bi-parametric grid of models whose results are valid in principle for any spiral galaxy of given maximum rotation velocity or total mass, and type T from 1 to 10.

The results include the time evolution of different regions of the disk and the halo along galactocentric distance, measured by the gas (atomic and molecular) and stellar masses, the star formation rate and chemical abundances of 15 elements. The present time radial distributions of diffuse and molecular gas and star formation rate surface

¹INTAS, 58, Avenue des Arts, 1000 Bruxelles, Belgium

densities, and of oxygen abundance - defined as $12 + \log(O/H)$ - are calculated and then compared with observational data.

One of the most important results of this work concerns the radial gradients of abundances. These are completely flat for the latest morphological types, from $T \sim 7$ to 10, with abundances $12 + \log(O/H) \sim 7.5 - 8$, while they appear steep for late type galaxies ($T \sim 4 - 7$), in comparison with earlier types. This is in agreement with observations and it resolves the apparent inconsistency in the trends giving larger gradients for later type galaxies while some irregulars show no gradient at all and very uniform abundances. The explanation resides in the star formation to infall ratio provided by the multiphase models.

These models are also able to explain the existing correlations between generic characteristics of galaxies and their radial distributions, as arising from variations in the characteristic infall rate and in the cloud and star formation efficiencies with galactic morphological type and/or Arm Class.

Subject headings: galaxies: abundances – galaxies: evolution – galaxies: spirals – galaxies: stellar content

1. Introduction

Early chemical evolution models (Lynden-Bell 1975; Tinsley 1980; Clayton 1987, 1988; Sommer-Larsen & Yoshii 1989) were developed with the aim of explaining the solar elemental abundances, now revised in Grevesse & Sauval (1998), and other characteristics observed in the Solar Neighborhood, such as the metallicity distribution (Pagel & Patchett 1975; Pagel 1990; Rocha-Pinto & Maciel 1996; Chang et al. 1999), the age-metallicity relation of stars or the star formation history (Twarog 1980; Carlbergh et al. 1985; Barry 1988; Rocha-Pinto et al. 2000a,b). Subsequently, the scope of the models was enlarged to include the whole Galactic Disk, in an attempt to reproduce the observed radial gradients in the abundances of oxygen, nitrogen and other elements, as deduced from HII regions and planetary nebulae (PN) observations (Peimbert 1979; Shaver et al. 1983) and of iron, as derived from data on stars and open clusters.

Variations of abundances with galactocentric distance have also been found, mainly from observations of HII regions, in other spirals (see Henry & Worthey 1999, and references therein), and the existence of abundance radial gradients in spiral disks has been firmly established.

From these data, several correlations have been found between the values of these gradients and galaxy characteristics, e.g. Vila-Costas & Edmunds (1992); Zaritsky, Kennicutt & Huchra (1994), where a first quantification of these trends was done. We can, thus, enumerate the following observational facts:

1. The central value of the abundance, as extrapolated from the obtained gradient, depends on

the morphological type with the earlier type galaxies showing larger central abundances than the later ones (Vila-Costas & Edmunds 1992; Zaritsky, Kennicutt & Huchra 1994).

2. The radial gradient in dex kpc^{-1} depends on the morphological type: late-type galaxies show steeper radial distributions of oxygen abundances than earlier ones, which show in some cases almost no gradient (Oey & Kennicutt 1993; Dutil & Roy 1999).
3. There is a correlation between abundance and total mass surface density, which, in turn, is related to the morphological type. This correlation is stronger when the total mass of the galaxy, including the bulge, instead of the mass of the exponential disk alone, is used (Ryder 1995).
4. A correlation exists between the atomic gas fraction and the oxygen abundance, which remains when the molecular gas component is also included, but only if this mass is estimated using a conversion factor χ of CO intensity to molecular gas density variable with metallicity in a way that produces a smooth radial distribution of gas (Vila-Costas & Edmunds 1992).
5. The fraction H_2/HI varies with the oxygen abundance, as it was suggested by Tosi & Díaz (1990).

From the point of view of theoretical models, the existence of these radial gradients can not be due only to the gas fraction radial distribution, and other effects must be invoked (Tinsley 1980; Götz & Köppen 1992; Köppen 1994). Thus, most recently computed models, including the multiphase model used in this work, assume a SFR law depending on galactocentric radius through a power law of the gas density. They also include the infall of gas whose rate varies with galactocentric radius. Therefore they follow the so-called *biased infall* hypothesis, where the disk forms in an inside/outside scenario. The physical reason for this is that the gas tends to collapse more quickly in the inner regions of the disk, the process being slower in the outer regions. These models are very similar in their hypotheses and results for the present time.

Most numerical models, although more sophisticated every time, have been historically checked only on the MWG or a fiducial galaxy as an example. There have been models computed to analyze irregular galaxies such as the Magellanic Clouds (Pagel & Tautvaisiene 1998) or IZw18. However, with the exception of Díaz & Tosi (1984) and Tosi & Díaz (1985), who modeled a sample of external spiral galaxies using rather simple assumptions about the star formation and infall rates, chemical evolution models have not been usually applied to other external large spirals. This prevents the adequate comparison of the correlations mentioned above with model results. This is the main purpose of this work.

The multiphase model we will use here, has been already used and checked against observational constraints not only for the Milky Way Galaxy, as it is commonly done, but also for a sample of spiral galaxies (disks and bulges) (Mollá, Ferrini & Díaz 1996; Mollá, Hardy & Beauchamp 1999; Mollá, Ferrini & Gozzi 2000) of different morphological types and total masses, and the observed

radial distributions of diffuse and molecular gas, oxygen abundances and star formation rate have been reproduced rather successfully.

The characteristics of the multiphase model have been described in Ferrini et al. (1992), Ferrini et al. (1994, –hereafter FMPD–), and Mollá & Ferrini (1995). It follows the two hypotheses above mentioned (SF and infall depending on the radius), as assumed in other works (Boissier & Prantzos 2000; Hou, Prantzos & Boissier 2000).

An advantage of using our model is that it includes a more realistic star formation. The usual SFR prescriptions are based in a Schmidt law, depending on the total gas surface density. Instead, the multiphase model assumes a star formation which takes place in two-steps: first, the formation of molecular clouds; then the formation of stars. This simulates a power law on the gas density with an exponent $n > 1$ with a threshold gas density as shown by Kennicutt (1989), and, more important, it allows the calculation of the two different gas phases present in the interstellar medium. In fact, the actual process of star formation, born by observations (Klessen 2001), is closer to our scenario with stars forming in regions where there are molecular clouds, than to the classical Schmidt law which depends only on the total gas density. Our assumed SFR implies that the some feedback mechanisms are included naturally and are sufficient to simulate the actually observed process of creation of stars from the interstellar medium.

To know the chemical evolution along the Hubble Sequence, that is, for spiral galaxies with different morphological types, we have also analyzed the observed correlations between the abundance gradients and galaxy characteristics. They are well reproduced for a reduced sample of galaxies (Mollá, Ferrini & Díaz 1996; Mollá & Roy 1999), and are interpreted as arising from variations in the characteristic infall rate and in the cloud and star formation efficiencies with galactic morphological type and/or Arm Class. However, some of these correlations may pose problems when the end of the Hubble Sequence is included. Thus, the mass-metallicity relation seems to be the same for bright spirals and low-mass irregular galaxies, but the correlation of a steep radial gradient of the oxygen abundance for galaxies of later types shows an effect on-off: when the galaxy mass decreases or the Hubble type changes to the latest irregulars, the steep radial gradient disappears and the abundance pattern becomes uniform for the whole disk (Walsh & Roy 1997), a result difficult to explain.

Besides that, the number of galaxies modeled until now is small (11) and restricted in morphological type (T varies between 3 and 7) and luminosity class (mostly bright spirals). This situation is unlikely to change since due to the method of modeling, by fitting a large number of constraints for every galaxy, it is not possible to model a large number of individual objects.

In order to extend our modeling to the whole parameter space, we have used the Universal Rotation Curve from Persic, Salucci & Steel (1996) to calculate a large number of radial mass distributions. These distributions, which are the fundamental input of the multiphase model, represent theoretical protogalaxies or initial structures which would evolve to form the observed disks or irregulars. The total mass of each simulated galaxy, besides its own effect on the galaxy

evolution, defines the characteristic collapse time scale or gas infall rate onto the disk. On the other hand we assume that the molecular cloud and star formation efficiencies are probabilities with values between 0 and 1 and thus, we select 10 different set of values. With this two hypotheses we construct a bi-parametric grid of 440 models simulating galaxies of 44 different total masses which may evolve, each one of them, at 10 different rates, which, as we will see, may be related on morphological types from $T=1$ to $T=10$.

This grid implies the computation of a large number of models, and extends our previous ones which were only applied to a reduced number of galaxies (11). With this new grid we analyze the evolution of galaxies having any possible combination of total mass and efficiencies to form stars and molecular clouds. Moreover, the statistical analysis of model results and their comparison with correlations may now be performed more adequately. These models could also be applied to theoretical galaxies resulting from self-consistent hydrodynamical numerical simulations thus following their subsequent chemical evolution.

With this series of models we try to study the time evolution of galaxies of different masses and morphological types. No attempt has been made, however, to explain how the morphological type sequence is produced. As we use a chemical evolution code, we cannot obtain any dynamical information, such as velocity dispersions, bulge sizes, or spiral pattern characteristics, necessary to determine the morphological type from our resulting galaxies. But we can, as we do, compare our results with data of actual galaxies of given morphological types and check if they are well reproduced.

In Section 2 we summarize the generic multiphase chemical evolution model characteristics and the strategy of its application to spirals of different types. We analyze our results in a general way in Section 3. In Section 4 we will show how the model results are in agreement with the observations for some individual galaxies. Finally, the conclusions of this work are presented in Section 5.

Our results, such as it occurs with most numerical calculations, at difference to analytical methods, have been until now only shown in a graphical way, thus making difficult their possible use by the scientific community not directly involved in the chemical evolution field. For this purpose all results obtained in this work will be available in electronic form at CDS via anonymous ftp to [cdsarc.u-strasbg.fr](ftp://cdsarc.u-strasbg.fr) (130.79.128.5) or via <http://cdsweb.u-strasbg.fr/Abstract.html>, or <http://pollux.ft.uam.es/astro/mercedes/grid> or upon request to authors.

2. The Generic Multiphase Model

In the generalization of this model we assume a protogalaxy to be a spheroid composed of primordial gas whose total mass and radial distribution $M(R)$ is calculated from its corresponding rotation curve. The Universal Rotation Curve from Persic, Salucci & Steel (1996, hereafter PSS) has been used for obtaining the required inputs to the models. These authors use a homogeneous

sample of about 1100 optical and radio rotation curves to estimate their profile and amplitude which are analyzed statistically. From this study, they obtain an expression for the rotation velocity:

$$V(R) = V(R_{opt}) \left\{ (0.72 + 0.44 \log \lambda) \frac{1.97x^{1.22}}{(x^2 + 0.61)^{1.43}} + 1.6e^{-0.4\lambda} \frac{x^2}{x^2 + 2.25\lambda^{0.4}} \right\}^{1/2} \text{ kms}^{-1} \quad (1)$$

where R_{opt} is the radius encompassing 83% of the total integrated light, given by the expression: $R_{opt} = 13(L/L_*^{0.5})$ kpc, $x = R/R_{opt}$ and $V(R_{opt})$ is the rotation velocity at the optical radius R_{opt} in kms^{-1} :

$$V(R_{opt}) = \frac{200\lambda^{0.41}}{[0.80 + 0.49 \log \lambda + (0.75e^{-0.4\lambda}) / (0.47 + 2.25\lambda^{0.4})]^{1/2}} \text{ kms}^{-1} \quad (2)$$

where the value λ represents L/L_* , with $L_* = 10^{10.4} L_\odot$.

In Table 1 we show the characteristics obtained with PSS96 equations for 44 different values of λ . In Column (1) we give the number of the radial distribution, defined by the value of λ , given in Column (2). The total integrated luminosity L and the corresponding magnitude in I-band are in Columns (3) and (4). The virial radius $R_{gal} = 14.8\lambda^{-0.14}R_{opt}$, the exponential disk scale length $R_D = R_{opt}/3.2$ and the characteristic radius, which we will use as our reference radius, defined for each radial distribution as $R_0 = R_{opt}/2$ are, in units of kpc, in Columns (5),(6) and (7), respectively. Column (8) shows the rotation velocity, in kms^{-1} , reached at a radius $R_M = 2.2R_D$ kpc. From this value we compute $\Omega_{max} = V_{max}/R_M$, given in Column (9), in $\text{kms}^{-1}\text{kpc}^{-1}$. The total mass of the galaxy, calculated with the classical expression $M_{gal} = 2.3210^5 R_{gal}V_{max}^2$, in units of $10^9 M_\odot$, is in Column (10), and the characteristic collapse time scale, in Gyr, which will be described below, corresponding to each distribution, is given in Column (11).

Each galaxy is divided into concentric cylindrical regions 1 kpc wide. From the corresponding rotation curves we calculate the radial distributions of total mass $M(R)$, and the total mass included in each one of cylinders $\Delta M(R)$. Both distributions are shown in Fig.1. The total mass includes the dark matter component (DM), which should not be considered, in principle, in the chemical evolution calculations. However, maximum disk models have been suggested by a number of papers (Palunas & Williams 2000; Sellwood & Kosowsky 2000, and references there in) for decomposition of masses in spiral galaxies. These works claim that 75% of the spiral galaxies are well fitted without a dark matter halo and that the failure to reproduce an other 20% is directly related to the existence of non-axisymmetric structures (bars or strong spiral arms). This implies that the contribution of DM seems to be negligible in the large massive galaxies, and more so in the inner parts of disks, where the chemical evolution takes place.

Once the mass distribution is given, the model calculates, separately, the time evolution of the halo and disk components belonging to each cylindrical region. The halo gas falls into the

Table 1. Galaxy Characteristics dependent on the Total Mass.

Num	λ	$\log L$ L_{\odot}	M_I	R_{gal} kpc	R_D kpc	R_0 kpc	V_{max} (kms $^{-1}$)	Ω_{max} (kms $^{-1}$ kpc $^{-1}$)	M_{gal} ($10^9 M_{\odot}$)	τ_0 (Gyr)
1	0.01	8.40	-16.53	36.7	0.4	0.7	30.	34.02	8.	60.37
2	0.02	8.70	-17.35	47.1	0.6	0.9	40.	31.95	18.	40.12
3	0.03	8.88	-17.83	54.4	0.7	1.1	48.	30.80	29.	31.59
4	0.04	9.00	-18.17	60.4	0.8	1.3	54.	30.01	40.	26.66
5	0.05	9.10	-18.43	65.4	0.9	1.5	59.	29.40	52.	23.38
6	0.06	9.18	-18.65	69.9	1.0	1.6	63.	28.92	65.	21.00
7	0.07	9.25	-18.83	73.9	1.1	1.7	67.	28.52	78.	19.17
8	0.08	9.30	-18.99	77.5	1.1	1.8	71.	28.18	91.	17.72
9	0.09	9.35	-19.13	80.9	1.2	1.9	75.	27.88	105.	16.53
10	0.10	9.40	-19.25	84.0	1.3	2.1	78.	27.61	119.	15.54
11	0.11	9.44	-19.36	86.9	1.3	2.2	81.	27.38	133.	14.69
12	0.12	9.48	-19.47	89.7	1.4	2.3	84.	27.16	147.	13.96
13	0.13	9.51	-19.56	92.3	1.5	2.3	87.	26.96	162.	13.31
14	0.14	9.55	-19.65	94.8	1.5	2.4	90.	26.78	176.	12.74
15	0.15	9.58	-19.73	97.2	1.6	2.5	92.	26.62	191.	12.24
16	0.16	9.60	-19.80	99.5	1.6	2.6	95.	26.46	207.	11.78
17	0.17	9.63	-19.88	101.7	1.7	2.7	97.	26.32	222.	11.37
18	0.18	9.66	-19.94	103.8	1.7	2.8	99.	26.18	237.	10.99
19	0.19	9.68	-20.01	105.8	1.8	2.8	101.	26.05	253.	10.64
20	0.20	9.70	-20.07	107.8	1.8	2.9	104.	25.93	269.	10.33
21	0.30	9.88	-20.55	124.7	2.2	3.6	122.	25.00	433.	8.13
22	0.40	10.00	-20.89	138.3	2.6	4.1	138.	24.35	608.	6.86
23	0.50	10.10	-21.15	149.9	2.9	4.6	151.	23.86	791.	6.02
24	0.60	10.18	-21.36	160.1	3.1	5.0	163.	23.47	981.	5.41
25	0.70	10.25	-21.55	169.2	3.4	5.4	173.	23.15	1176.	4.94
26	0.80	10.30	-21.70	177.5	3.6	5.8	183.	22.87	1377.	4.56
27	0.90	10.35	-21.84	185.2	3.9	6.2	192.	22.63	1582.	4.26
28	1.00	10.40	-21.97	192.4	4.1	6.5	200.	22.41	1791.	4.00
29	1.10	10.44	-22.08	199.1	4.3	6.8	208.	22.22	2004.	3.78
30	1.20	10.48	-22.18	205.5	4.5	7.1	216.	22.04	2220.	3.59
31	1.30	10.51	-22.28	211.5	4.6	7.4	223.	21.88	2440.	3.43
32	1.40	10.55	-22.36	217.2	4.8	7.7	230.	21.74	2663.	3.28
33	1.50	10.58	-22.45	222.6	5.0	8.0	236.	21.60	2888.	3.15
34	1.60	10.60	-22.52	227.9	5.1	8.2	243.	21.48	3117.	3.03
35	1.70	10.63	-22.59	232.9	5.3	8.5	249.	21.36	3347.	2.93
36	1.80	10.66	-22.66	237.7	5.5	8.7	255.	21.25	3581.	2.83
37	1.90	10.68	-22.72	242.4	5.6	9.0	260.	21.15	3816.	2.74
38	2.00	10.70	-22.79	246.9	5.7	9.2	266.	21.05	4054.	2.66
39	2.50	10.80	-23.05	267.6	6.4	10.3	291.	20.63	5274.	2.33
40	3.00	10.88	-23.26	285.7	7.0	11.3	314.	20.29	6539.	2.09
41	3.50	10.94	-23.45	302.0	7.6	12.2	335.	20.01	7843.	1.91
42	4.00	11.00	-23.60	316.9	8.1	13.0	353.	19.77	9180.	1.77
43	4.50	11.05	-23.74	330.6	8.6	13.8	371.	19.56	10548.	1.65
44	5.00	11.10	-23.87	343.4	9.1	14.5	387.	19.37	11944.	1.55

Note. — Column 1 is the number of the radial distribution, defined by the value of $\lambda = L/L_*$ ($L_* = 10^{10.4} L_{\odot}$), given in Column (2). Columns (3) and (4) are the total integrated luminosity L , in logarithmic scale, and the corresponding magnitude in I-band. The virial radius $R_{gal} = 14.8\lambda^{-0.14} R_{opt}$, the exponential disk scale length $R_D = R_{opt}/3.2$ and the characteristic radius, defined as $R_0 = R_{opt}/2$ are, in units of kpc, in Columns (5),(6) and (7), respectively. Column (8) shows the rotation velocity, in kms $^{-1}$, reached at a radius $R_M = 2.2R_D$ kpc. $\Omega_{max} = V_{max}/R_M$, is given in Column (9) in kms $^{-1}$ kpc $^{-1}$. The total mass of the galaxy $M_{gal} = 2.3210^5 R_{gal} V_{max}^2$, in units of $10^9 M_{\odot}$, is in Column (10), and the characteristic collapse time scale, in Gyr, is given in Column (11)

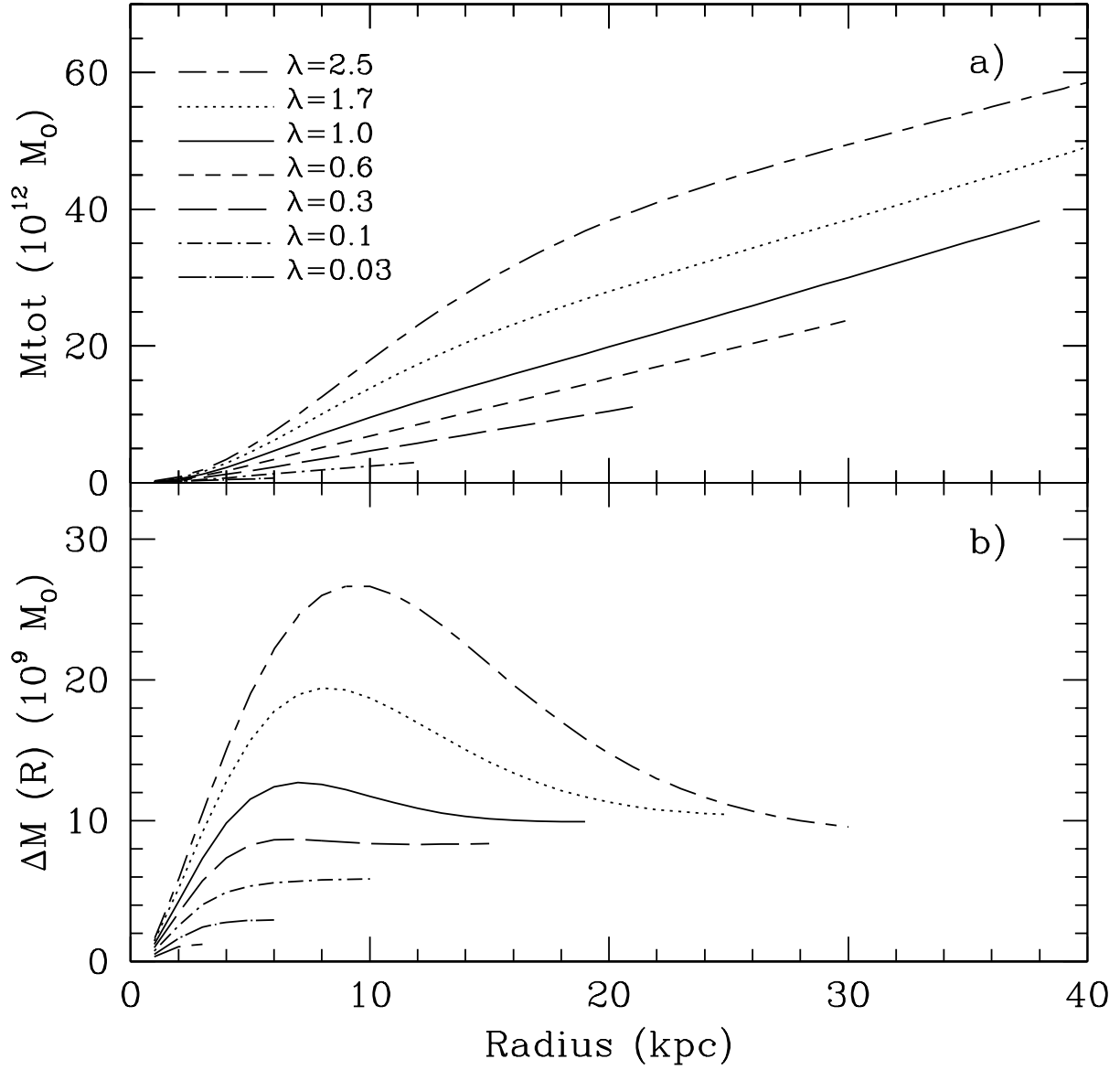


Fig. 1.— Radial distributions: a) total masses M_{tot} , b) masses $\Delta M(R)$ included in our cylinders, for different values of λ following the labels in the figure.

equatorial plane to form out the disk, which is a secondary structure, created by the gravitational accumulation of this gas. The gas infall from the halo is parameterized by fg_H , where g_H is the gas mass of the halo and f is the infall rate, the inverse of the collapse time scale τ .

The total mass, computed for each rotation curve, defines the characteristic collapse time scale for each galaxy, through the expression: $\tau_0 \propto M_9^{-1/2}T_9$ (Gallagher, Hunter & Tutukov 1984), where M_9 is the total mass of the galaxy in $10^9 M_\odot$ and T_9 is its age, assumed 13 Gyr in all cases. From the ratio of the corresponding total mass of a given galaxy and the MWG, and after calibration with the MWG model, we obtain a value τ_0 for each spiral galaxy:

$$\tau_0 = \tau_\odot (M_9, gal / M_{9, MWG})^{-1/2} \quad (3)$$

We would like emphasize that the characteristic collapse time scale computed with Equation 3 is not a free-fall time but has been calculated through calibration with the Milky Way value, $\tau_\odot \sim 4 - 6$ Gyr, determined in Ferrini et al. (1992) and very similar to that found in other standard Galactic chemical evolution models. This value is constrained by using a large number of data, such as the ratio of the halo to disk mass, M_{halo}/M_{disk} , the relation of [O/Fe] vs [Fe/H] for stars in the halo and in the disk, and the present infall rate, ($0.7 M_\odot \text{pc}^{-2} \text{Gyr}^{-1}$ Mirabel 1989), which are well reproduced by this long scale to form the disk.

The mass which does not fall will remain in the halo, thus yielding a ratio M_{halo}/M_{disk} for the baryonic component which is also in agreement with observations. The relative normalization of halo, thick and thin disk surface mass densities in the galactic plane (Sandage 1987) gives a proportion 1: 22: 200, which implies that the halo surface mass density must be 1/100 of that of the disk component. This result is in agreement with the ratio obtained by the multiphase model (Ferrini et al. 1992; Pardi & Ferrini 1995).

This collapse time scale also includes dynamical effects and is, therefore, longer than a simple free-fall time (≤ 1 Gyr for the MWG). By using this method to compute the characteristic collapse time scale for spiral galaxies with masses different from our own, we are taking into account the gravitational effect, although we are neglecting dynamical effects that may be different from those of the MWG.

The characteristic time scales for our models, τ_0 , are shown in Fig. 2a) vs the rotation velocity at the optical radius for each galaxy. Solid dots are the values used in our previous models for individual spiral galaxies (Ferrini et al- 1994; Mollá, Ferrini & Díaz 1996; Mollá, Hardy & Beauchamp 1999). τ_0 is defined for every galaxy as being that corresponding to the region located at R_0 defined above and given in Column (7) of Table 1.

An important consequence of the hypothesis linking the collapse time scale with the radial distribution of the total mass, is that low mass galaxies take more time to form their disks, in apparent contradiction with the standard hierarchical picture of galaxy formation. We are in agreement with Boissier & Prantzos (2000) that this characteristic is, however, essential to reproduce most observational features along the Hubble Sequence, as the metallicity-magnitude relations or the colors

of disks.

It is evident that, following the same relation between collapse time scale and mass, this collapse time scale must be variable with galactocentric radius. If we assume that the total mass surface density has an exponential form as the surface brightness, the collapse time scale required to obtain that shape should depend on radius through an exponential function, which increases with a scale length $\lambda_D \propto Re$ (where Re is the corresponding scale length of the surface brightness radial distribution). We must bear in mind, however, that the surface brightness distribution is the final result of the combination of both the collapse and the star formation processes, and therefore the collapse time scale may have in principle a different dependence on radius than the surface brightness itself. Nevertheless, for simplicity, we assume the collapse time scale as an exponential function variable along the radius with a scale length λ_D which we assume equal to the $R_D/2$ given by PSS96:

$$\tau_{coll}(R) = \tau_0 \exp((R - R_0)/\lambda_D) \quad (4)$$

This means that the scale length decreases for the later type of galaxies and is larger for the earlier ones. This is in agreement with observations from Simien & de Vaucouleurs (1986, see their Fig. 4), and has been more recently found by Graham & de Block (2001) –but also see Fig. 2 from Guzmán et al. (1996).

The radial dependence of the infall rate is not imposed *a priori* in our scenario: it is consequence of the gravitational law and of the total mass distribution in the protogalaxy. The physical meaning is clear: galaxies begin to form their inner regions before the outer ones in a classical inside-out scheme. This halo-disk connection is crucial for the understanding of the evolution of a galaxy from early times, the inside-out scenario resulting essential to reproduce the radial gradient of abundances (Portinari & Chiosi 1999; Boissier & Prantzos 2000). In fact, when the dynamical equations are also taken into account in a chemo-dynamical model (Samland, Hensler & Theis 1997), this scenario is produced naturally; thus our model yields results in good agreement with more sophisticated models.

The radial variation of the collapse time scale for each galaxy, calculated with equation (4) is shown in Fig.2b), where we also draw a solid line at the 13 Gyr, the assumed age of galaxies. If the collapse time scale is larger than this value, there is not enough time for all the gas to fall onto the disk: only a small part of it has moved from the halo to the equatorial plane and the disk formation is not yet complete. This might explain the data from Sancisi et al. (2001), who have found an extended component of H I, different from the cold disk, located in the halo, rotating more slowly than the disk and with radial inward motion.

In the various regions of the disk or bulge, and the halo, which treat separately, we allow for different phases of matter aggregation: diffuse gas (g), clouds (c , except in the halo), low-mass ($s_1, m < 4M_\odot$) and massive stars ($s_2, m \geq 4M_\odot$), and remnants. This border mass is related to

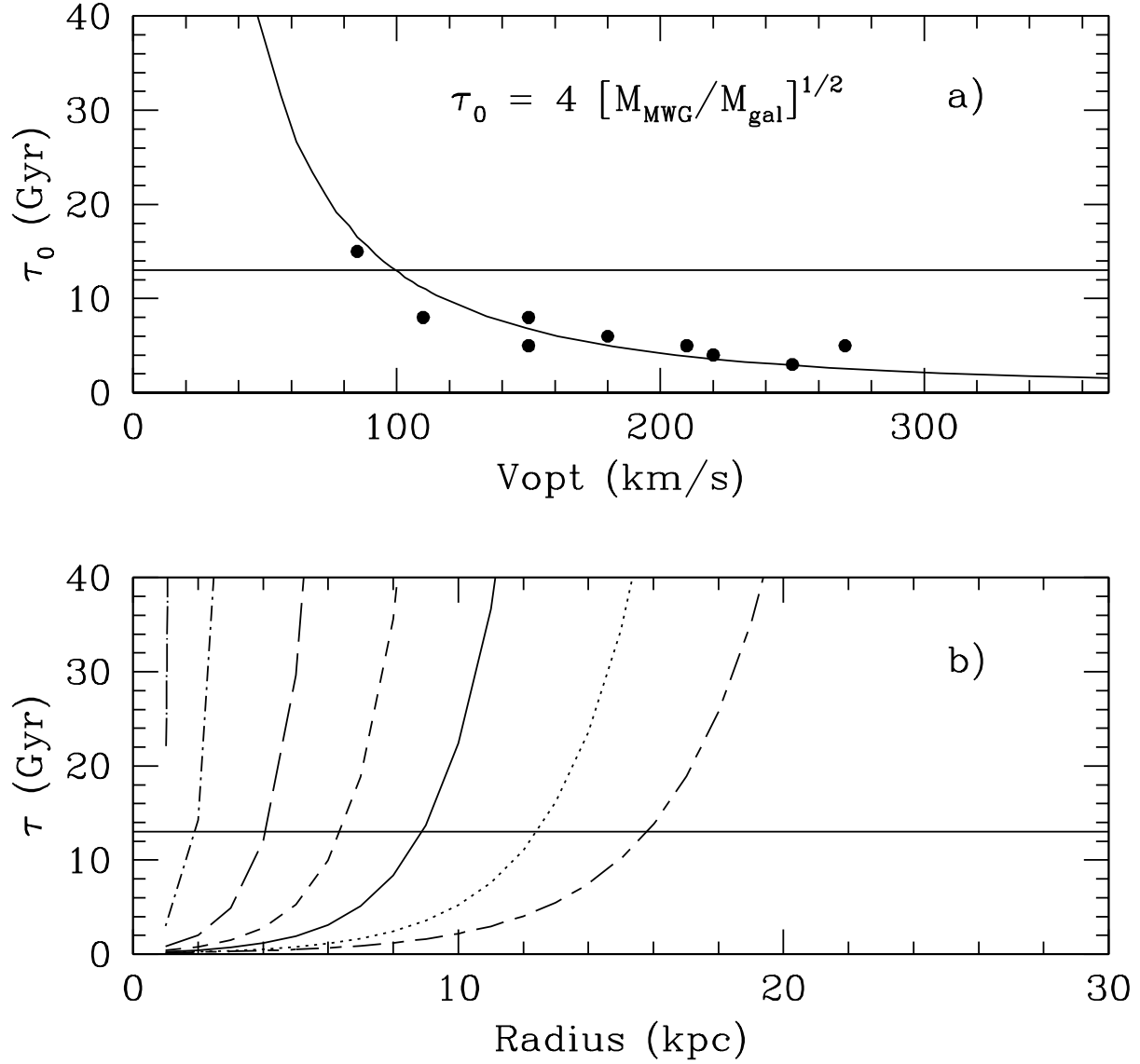


Fig. 2.— a) Characteristic collapse timescale τ_0 for each galaxy according to the maximum rotation velocity. b) Radial distribution of the collapse times scales $\tau_{coll}(R)$. Lines have the same meaning than in Fig. 1 The horizontal solid line represents the assumed age of galaxies, 13 Gyr.

nucleosynthesis prescriptions: stars with masses lower than $4 M_{\odot}$ only produce light elements, and do not contribute to the interstellar medium enrichment. ²

The mass in the different phases of each region changes by the following conversion processes:

1. Star formation by the gas-spontaneous fragmentation in the halo: $\propto K g_H^{1.5}$ (a Schmidt law with $n = 1.5$)
2. Cloud formation in the disk from diffuse gas: $\propto \mu g_D^{1.5}$
3. Star formation in the disk from cloud-cloud collisions: $\propto H c^2$
4. Induced Star formation in the disk *via* massive star-cloud interactions: $\propto a c s_2$
5. Diffuse gas restitution from these cloud and star formation processes

where K , μ , H and a , besides the parameter f or τ_0 already defined, are the parameters of the model.

Since the number of parameters is high, we have followed a precise strategy to reduce to a minimum their degree of freedom. Actually, not all input parameters in our models can be considered as free. The parameter f is the inverse of the collapse time scale, which, in turn, is defined by each mass radial distribution, as we have explained above.

The other parameters, (K , μ , H and a) are calculated for each radial region from the equations given in Ferrini et al- (1994), which give their dependence on the region volume ³ through proportionality factors or *efficiencies*. These efficiencies are the probabilities of cloud formation, ϵ_{μ} , of cloud—cloud collision, ϵ_H , of the interaction of massive stars with clouds, ϵ_a in the disk, and the efficiency to form stars in the halo, ϵ_K , and are characteristic of each spiral galaxy.

The term associated to the induced star formation describes a local process and, as a result, its coefficient ϵ_a is considered independent of both position and morphological type. The term ϵ_K is also assumed constant for all halos, thus being independent of morphological type ⁴. Both efficiencies take therefore the same values already used in our previous model for the MWG, for all our 440 models.

The fact that galaxies with the same gravitational potential or mass and different morphological type or appearance exist, implies that the evolution of a galaxy does not depend solely on

²On the other hand, this discrimination in two groups, less and more massive than $4 M_{\odot}$, allow a very easy comparison of our resulting metallicity distribution with the observed one, based in G-dwarf low mass stars.

³The volume of the disk is calculated with a scale height of 0.2 kpc for all galaxies

⁴The volume of the halo for each concentric region, which has also an effect on the value of the parameter K , is computed through the expression: $V_{\text{halo}}(R) = 2R_{\text{halo}}R\sqrt{(1 - \frac{R}{R_{\text{halo}}})^2}$. Since $R_{\text{halo}} = 2.5R_{\text{opt}}$, V_{halo} takes a different value for each mass radial distribution, but does not change with morphological type.

gravitation, but also on certain dynamical conditions. These conditions cannot be taken into account, obviously, in a simple chemical evolution model, but may change the evolution of a galaxy, (mostly the star formation rate through the temperature variations). They are included in our efficiencies to form molecular clouds and stars, ϵ_μ and ϵ_H , which are allowed to change from one galaxy to another.

Therefore, we assume that ϵ_μ and ϵ_H vary between 0 and 1. Ten different values in this range are taken for each radial mass distribution, in order to reproduce different rates of evolution. We thus obtain all possible combinations of collapse time scale with star and molecular cloud formation efficiencies.

On the other hand, we know by our previous works that these efficiencies change with galaxy morphological type. Thus, as we can see in Fig. 3, the values used for some spiral galaxies in Mollá, Ferrini & Díaz (1996); Mollá, Hardy & Beauchamp (1999), shown as full dots in both panels, depend on the morphological type of these galaxies. In fact, this dependence was already found in Ferrini & Galli (1988); Galli & Ferrini (1989), where, these authors quantified the efficiencies to form molecular clouds and the frequency of cloud-cloud collisions, finding that a variation of 10 in the parameters H and μ is needed when the Hubble type changes from one stage to the next (Sa to Sb, etc..). They based their work in the particle simulations of a clumpy interstellar medium from Roberts & Hausman (1984) and Hausman & Roberts (1984).

Therefore, by taking into account the probability nature of our efficiencies, we fit a probability function to the previous model values:

$$\epsilon_\mu = \exp(-T^2/20) \tag{5}$$

$$\epsilon_H = \exp(-T^2/8) \tag{6}$$

These functions are shown as solid lines in Fig.3, where the points represent our previous model efficiencies. With these functions we have computed 10 values for ϵ_μ and ϵ_H , which we may relate to galaxy morphological type. We must make clear that this correspondence comes as a result from our (previous) models. However, we may have simply considered 10 different values computed with a probability function $\exp(-x^2/a)$ in the range [0,1]. We could have then checked the equivalence between x and T *a posteriori*.

Besides that, we have checked that these efficiencies take values according to the estimations obtained from observed star forming regions for some particular galaxies. Thus, the conversion of atomic to molecular gas in NGC 224 is approximately 50% (Lada et al. 1988), what implies $\epsilon_\mu = 0.50$ in excellent agreement with the value used for the model of this galaxy. In the same way, for NGC 598, Wilson et al. (1988) estimated the mean time to consume the molecular gas in 1.1 Gyr and for the total gas in 1.4 Gyr, that correspond to values $\epsilon_\mu \sim 0.05$ and $\epsilon_H \sim 0.01$, similar to

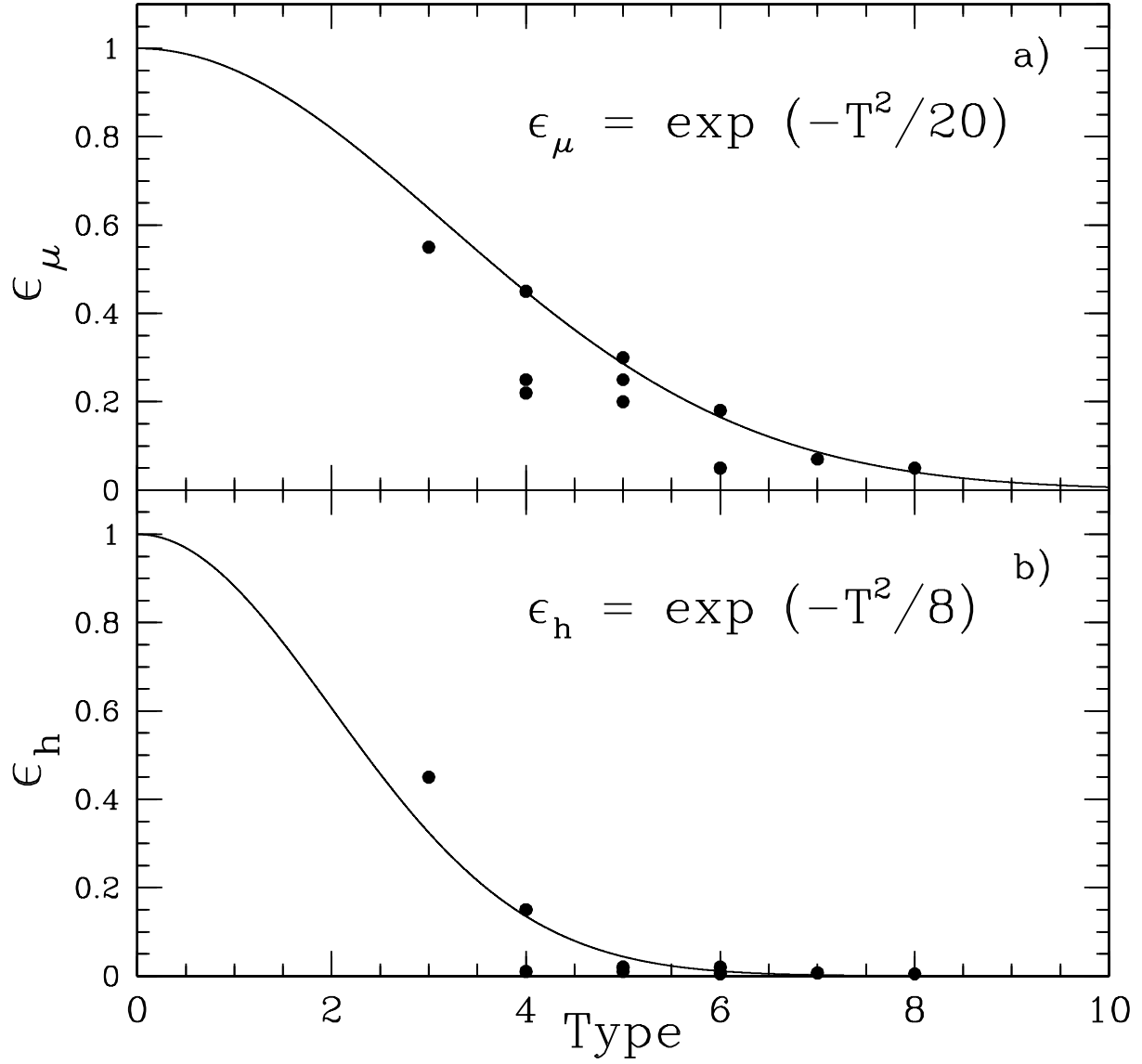


Fig. 3.— Dependence of the efficiencies, ϵ_μ and ϵ_H on morphological type T. The line is the fit performed to the values used in our previous models, represented by solid dots

those used in Mollá, Ferrini & Díaz (1996). Thus, our assumptions are supported by observational studies.

Summarizing, only the characteristic collapse time scale, depending on the total mass, and these two efficiencies, ϵ_μ and ϵ_H depending on morphological type, are varied from galaxy to galaxy.

The enriched material proceeds from the restitution from dying stars, considering their nucleosynthesis, their IMF (and the delayed restitution) and their final fate, via a quiet evolution, or Type I and II supernova explosions. Nucleosynthesis yields are taken from Woosley & Weaver (1995) for massive stars. For low mass and intermediate stars we use the set of yields from Renzini & Voli (1981). For the type I supernova explosion releases we take the model W7 from Nomoto, Thielemann & Yokoi (1984), as revised by Iwamoto et al. (1999).

Most recent works support the idea that the IMF is practically universal in space and constant in time (Wyse 1997; Scalo 1998; Meyer et al. 2000), showing only local differences. The adopted initial mass function (IMF) is taken from Ferrini, Palla & Penco (1990), very similar to a Scalo’s law and in a good agreement with the most recent data from Kroupa (2001), as we can see in Fig. 4.

3. Grid of Models: Presentation and Analysis

With the model computed following the previous section, we obtain 440 different time evolutions, 10 for each radial distribution cited in Table 1. The results corresponding to the mass of each region and phase, the star formation rate and the supernova rates, for these 440 models are shown in Tables 2, and 3. The elemental abundances for the disk are shown in Table 4. Here we only show, as an example, the results of the model corresponding to the radial distribution number 19 and $T = 5$ for the first and last Gyr. In Table 2 we list the time, in Gyr, in Column (1), and the galactocentric distance R , in kpc, in Column (2). Columns (3) to (9) give the masses, in $10^9 M_\odot$, in each region and phase: (3) the total mass in each region, (4) the mass of the disk region, (5) the mass in the diffuse gas phase, (6) the molecular gas, (7) the mass in low and intermediate mass stars, (8) the mass in massive stars and (9) the mass in remnants.

In Table 3, we show for each time step in Gyr, column (1), and radial distance, in kpc, column (2), the star formation rate, in units of $M_\odot yr^{-1}$, in the disk and the halo regions in Columns 3 and 4. The supernova rates, Types Ia and II, are in columns (5) and (6), for the disk and (7) and (8) for the halo, respectively, in units of $100 yr^{-1}$.

The abundances in the disk for 15 elements are shown in Table 4 also for each time in Gyr, column (1), and galactocentric distance, column (2): H, D, ^3He , ^4He , ^{12}C , ^{13}C , N, O, Ne, Si, S, Ca, and Fe are in columns from (3) to (16), respectively. All of them are given by mass.

The complete tables with the complete time evolution from 0 to 13 Gyr, with a time step of 0.5 Gyr, for the whole set of models may be obtained from <http://cdsweb.u-strasbg.fr/Abstract.html>

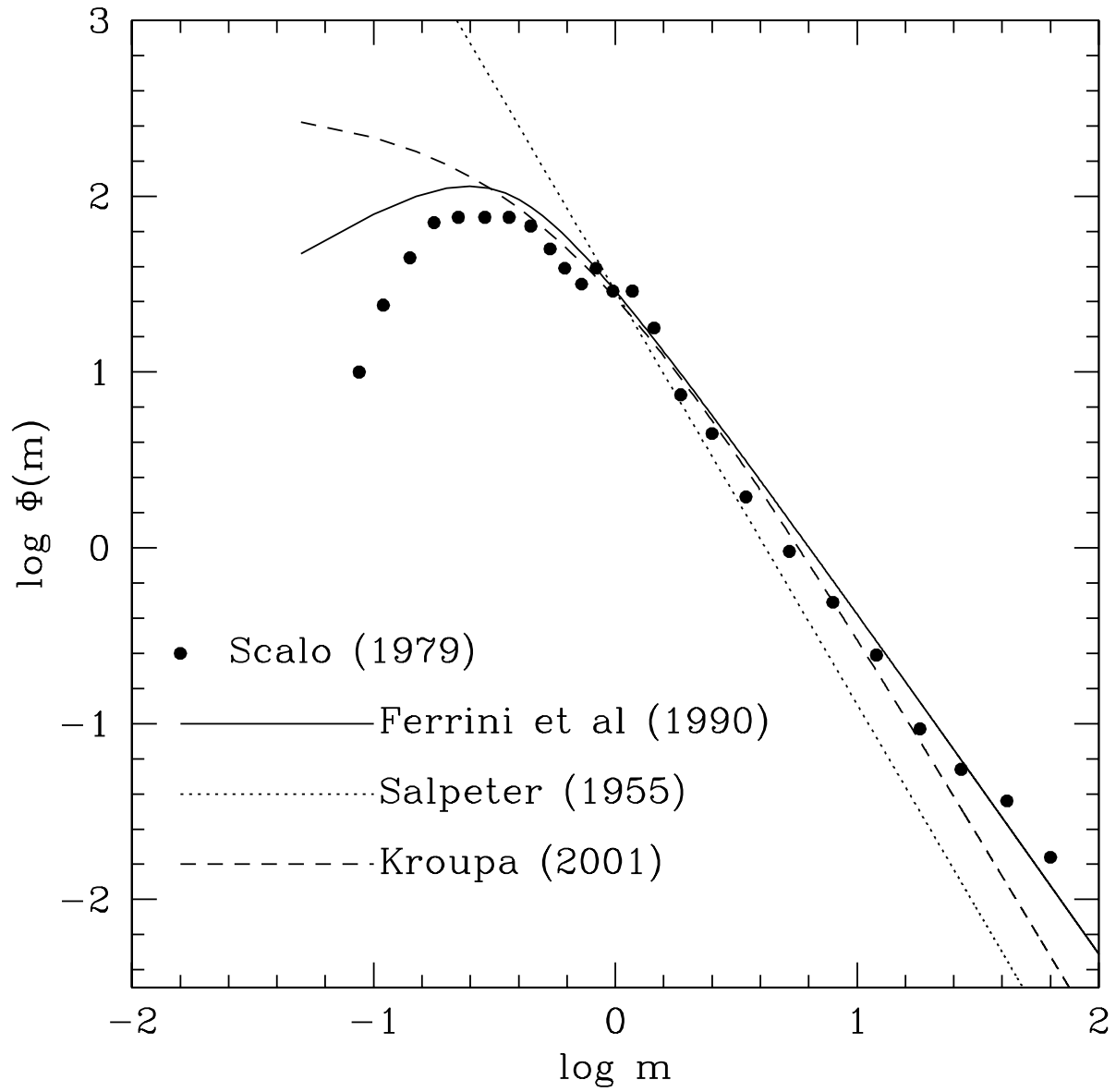


Fig. 4.— The IMF from Ferrini, Palla & Penco (1990), solid line, compared to a Salpeter law, dotted line, and that corresponding to Kroupa (2001), short-dashed line. Solid symbols correspond to Scalo (1986).

or <http://pollux.ft.uam.es/astro/mercedes/gridhttp> or upon request to authors.

Table 2. Model Results corresponding to masses in each region and phase.

Time Gyr	R kpc	Mtot ($10^9 M_\odot$)	Mdisk ($10^9 M_\odot$)	Mgas(HI) ($10^9 M_\odot$)	Mgas(H ₂) ($10^9 M_\odot$)	Mstars(M < 4M _⊙) ($10^9 M_\odot$)	Mstars(M ≥ 4M _⊙) ($10^9 M_\odot$)	Mremnants ($10^9 M_\odot$)
0.0	10.	0.44E+01	0.00E+00	0.10E-05	0.00E+00	0.00E+00	0.00E+00	0.00E+00
0.0	9.	0.45E+01	0.00E+00	0.10E-05	0.00E+00	0.00E+00	0.00E+00	0.00E+00
0.0	8.	0.45E+01	0.00E+00	0.10E-05	0.00E+00	0.00E+00	0.00E+00	0.00E+00
0.0	7.	0.44E+01	0.00E+00	0.10E-05	0.00E+00	0.00E+00	0.00E+00	0.00E+00
0.0	6.	0.43E+01	0.00E+00	0.10E-05	0.00E+00	0.00E+00	0.00E+00	0.00E+00
0.0	5.	0.42E+01	0.00E+00	0.10E-05	0.00E+00	0.00E+00	0.00E+00	0.00E+00
0.0	4.	0.39E+01	0.00E+00	0.10E-05	0.00E+00	0.00E+00	0.00E+00	0.00E+00
0.0	3.	0.32E+01	0.00E+00	0.10E-05	0.00E+00	0.00E+00	0.00E+00	0.00E+00
0.0	2.	0.21E+01	0.00E+00	0.10E-05	0.00E+00	0.00E+00	0.00E+00	0.00E+00
0.0	1.	0.60E+00	0.00E+00	0.10E-05	0.00E+00	0.00E+00	0.00E+00	0.00E+00
0.5	10.	0.44E+01	0.60E-04	0.64E-04	0.80E-07	0.19E-14	0.72E-16	0.21E-16
0.5	9.	0.45E+01	0.20E-03	0.20E-03	0.50E-06	0.78E-13	0.29E-14	0.85E-15
0.5	8.	0.45E+01	0.61E-03	0.61E-03	0.32E-05	0.34E-11	0.13E-12	0.37E-13
0.5	7.	0.44E+01	0.19E-02	0.18E-02	0.21E-04	0.15E-09	0.59E-11	0.17E-11
0.5	6.	0.43E+01	0.57E-02	0.55E-02	0.14E-03	0.73E-08	0.27E-09	0.79E-10
0.5	5.	0.42E+01	0.17E-01	0.16E-01	0.90E-03	0.35E-06	0.13E-07	0.38E-08
0.5	4.	0.39E+01	0.48E-01	0.42E-01	0.56E-02	0.16E-04	0.57E-06	0.17E-06
0.5	3.	0.32E+01	0.12E+00	0.92E-01	0.29E-01	0.54E-03	0.19E-04	0.62E-05
0.5	2.	0.21E+01	0.23E+00	0.13E+00	0.95E-01	0.83E-02	0.26E-03	0.11E-03
0.5	1.	0.60E+00	0.18E+00	0.64E-01	0.10E+00	0.18E-01	0.48E-03	0.26E-03
1.0	10.	0.44E+01	0.13E-03	0.13E-03	0.44E-06	0.12E-12	0.27E-14	0.19E-14
1.0	9.	0.45E+01	0.39E-03	0.39E-03	0.28E-05	0.48E-11	0.11E-12	0.81E-13
1.0	8.	0.45E+01	0.12E-02	0.12E-02	0.18E-04	0.21E-09	0.48E-11	0.35E-11
1.0	7.	0.44E+01	0.37E-02	0.36E-02	0.12E-03	0.94E-08	0.22E-09	0.16E-09
1.0	6.	0.43E+01	0.11E-01	0.11E-01	0.74E-03	0.43E-06	0.97E-08	0.73E-08
1.0	5.	0.42E+01	0.34E-01	0.29E-01	0.46E-02	0.19E-04	0.41E-06	0.32E-06
1.0	4.	0.39E+01	0.95E-01	0.69E-01	0.25E-01	0.67E-03	0.14E-04	0.12E-04
1.0	3.	0.32E+01	0.24E+00	0.13E+00	0.93E-01	0.14E-01	0.24E-03	0.27E-03
1.0	2.	0.21E+01	0.44E+00	0.16E+00	0.18E+00	0.92E-01	0.12E-02	0.22E-02
1.0	1.	0.60E+00	0.31E+00	0.66E-01	0.14E+00	0.11E+00	0.99E-03	0.28E-02

Table 2—Continued

Time Gyr	R kpc	Mtot ($10^9 M_\odot$)	Mdisk ($10^9 M_\odot$)	Mgas(HI) ($10^9 M_\odot$)	Mgas(H ₂) ($10^9 M_\odot$)	Mstars(M < 4M _⊙) ($10^9 M_\odot$)	Mstars(M ≥ 4M _⊙) ($10^9 M_\odot$)	Mremnants ($10^9 M_\odot$)
...
12.0	10.	0.44E+01	0.14E-02	0.12E-02	0.18E-03	0.21E-06	0.51E-09	0.15E-07
12.0	9.	0.45E+01	0.44E-02	0.34E-02	0.99E-03	0.73E-05	0.17E-07	0.53E-06
12.0	8.	0.45E+01	0.13E-01	0.84E-02	0.48E-02	0.21E-03	0.43E-06	0.16E-04
12.0	7.	0.44E+01	0.41E-01	0.20E-01	0.17E-01	0.37E-02	0.60E-05	0.32E-03
12.0	6.	0.43E+01	0.12E+00	0.45E-01	0.41E-01	0.33E-01	0.37E-04	0.34E-02
12.0	5.	0.42E+01	0.35E+00	0.86E-01	0.76E-01	0.17E+00	0.14E-03	0.20E-01
12.0	4.	0.39E+01	0.92E+00	0.13E+00	0.12E+00	0.59E+00	0.36E-03	0.79E-01
12.0	3.	0.32E+01	0.18E+01	0.13E+00	0.13E+00	0.13E+01	0.56E-03	0.20E+00
12.0	2.	0.21E+01	0.19E+01	0.51E-01	0.85E-01	0.15E+01	0.27E-03	0.27E+00
12.0	1.	0.60E+00	0.59E+00	0.57E-02	0.24E-01	0.46E+00	0.32E-04	0.97E-01
12.5	10.	0.44E+01	0.15E-02	0.13E-02	0.19E-03	0.26E-06	0.62E-09	0.19E-07
12.5	9.	0.45E+01	0.45E-02	0.35E-02	0.11E-02	0.90E-05	0.20E-07	0.68E-06
12.5	8.	0.45E+01	0.14E-01	0.86E-02	0.51E-02	0.25E-03	0.49E-06	0.20E-04
12.5	7.	0.44E+01	0.43E-01	0.20E-01	0.18E-01	0.42E-02	0.64E-05	0.38E-03
12.5	6.	0.43E+01	0.13E+00	0.46E-01	0.42E-01	0.36E-01	0.38E-04	0.38E-02
12.5	5.	0.42E+01	0.37E+00	0.87E-01	0.76E-01	0.18E+00	0.14E-03	0.22E-01
12.5	4.	0.39E+01	0.95E+00	0.13E+00	0.11E+00	0.62E+00	0.35E-03	0.85E-01
12.5	3.	0.32E+01	0.18E+01	0.13E+00	0.13E+00	0.14E+01	0.54E-03	0.21E+00
12.5	2.	0.21E+01	0.19E+01	0.49E-01	0.81E-01	0.15E+01	0.25E-03	0.28E+00
12.5	1.	0.60E+00	0.59E+00	0.55E-02	0.23E-01	0.46E+00	0.29E-04	0.10E+00
13.0	10.	0.44E+01	0.15E-02	0.13E-02	0.21E-03	0.32E-06	0.74E-09	0.24E-07
13.0	9.	0.45E+01	0.47E-02	0.35E-02	0.12E-02	0.11E-04	0.24E-07	0.85E-06
13.0	8.	0.45E+01	0.15E-01	0.87E-02	0.55E-02	0.30E-03	0.56E-06	0.24E-04
13.0	7.	0.44E+01	0.44E-01	0.21E-01	0.18E-01	0.48E-02	0.69E-05	0.44E-03
13.0	6.	0.43E+01	0.13E+00	0.46E-01	0.43E-01	0.39E-01	0.39E-04	0.43E-02
13.0	5.	0.42E+01	0.38E+00	0.87E-01	0.76E-01	0.19E+00	0.14E-03	0.24E-01
13.0	4.	0.39E+01	0.98E+00	0.13E+00	0.11E+00	0.64E+00	0.35E-03	0.92E-01
13.0	3.	0.32E+01	0.19E+01	0.12E+00	0.13E+00	0.14E+01	0.52E-03	0.23E+00
13.0	2.	0.21E+01	0.19E+01	0.46E-01	0.78E-01	0.15E+01	0.23E-03	0.29E+00

Table 2—Continued

Time Gyr	R kpc	Mtot ($10^9 M_\odot$)	Mdisk ($10^9 M_\odot$)	Mgas(HI) ($10^9 M_\odot$)	Mgas(H ₂) ($10^9 M_\odot$)	Mstars(M < 4M _⊙) ($10^9 M_\odot$)	Mstars(M ≥ 4M _⊙) ($10^9 M_\odot$)	Mremnants ($10^9 M_\odot$)
13.0	1.	0.60E+00	0.59E+00	0.53E-02	0.23E-01	0.46E+00	0.28E-04	0.10E+00

Table 3. Model Results: Star Formation Histories and Supernova Rates.

Time Gyr	R kpc	SFR(disk) $M_{\odot}yr^{-1}$	SFR(halo) $M_{\odot}yr^{-1}$	SN-Ia (disk) $100yr^{-1}$	SN-II (disk) $100yr^{-1}$	SN-Ia (halo) $100yr^{-1}$	SN-II(halo) $100yr^{-1}$
0.0	10.	0.00E+00	0.00E+00	0.00E+00	0.00E+00	0.00E+00	0.00E+00
0.0	9.	0.00E+00	0.00E+00	0.00E+00	0.00E+00	0.00E+00	0.00E+00
0.0	8.	0.00E+00	0.00E+00	0.00E+00	0.00E+00	0.00E+00	0.00E+00
0.0	7.	0.00E+00	0.00E+00	0.00E+00	0.00E+00	0.00E+00	0.00E+00
0.0	6.	0.00E+00	0.00E+00	0.00E+00	0.00E+00	0.00E+00	0.00E+00
0.0	5.	0.00E+00	0.00E+00	0.00E+00	0.00E+00	0.00E+00	0.00E+00
0.0	4.	0.00E+00	0.00E+00	0.00E+00	0.00E+00	0.00E+00	0.00E+00
0.0	3.	0.00E+00	0.00E+00	0.00E+00	0.00E+00	0.00E+00	0.00E+00
0.0	2.	0.00E+00	0.00E+00	0.00E+00	0.00E+00	0.00E+00	0.00E+00
0.0	1.	0.00E+00	0.00E+00	0.00E+00	0.00E+00	0.00E+00	0.00E+00
0.5	10.	0.00E+00	0.74E-01	0.12E-14	0.68E-13	0.28E-01	0.23E+00
0.5	9.	0.00E+00	0.75E-01	0.50E-13	0.28E-11	0.28E-01	0.23E+00
0.5	8.	0.00E+00	0.77E-01	0.22E-11	0.12E-09	0.29E-01	0.24E+00
0.5	7.	0.00E+00	0.79E-01	0.99E-10	0.55E-08	0.30E-01	0.24E+00
0.5	6.	0.00E+00	0.82E-01	0.47E-08	0.26E-06	0.31E-01	0.25E+00
0.5	5.	0.40E-05	0.83E-01	0.22E-06	0.12E-04	0.31E-01	0.25E+00
0.5	4.	0.19E-03	0.80E-01	0.10E-04	0.53E-03	0.31E-01	0.24E+00
0.5	3.	0.62E-02	0.67E-01	0.36E-03	0.17E-01	0.26E-01	0.20E+00
0.5	2.	0.79E-01	0.37E-01	0.60E-02	0.23E+00	0.16E-01	0.11E+00
0.5	1.	0.13E+00	0.56E-02	0.14E-01	0.38E+00	0.29E-02	0.17E-01
1.0	10.	0.00E+00	0.73E-01	0.89E-13	0.22E-11	0.51E-01	0.22E+00
1.0	9.	0.00E+00	0.74E-01	0.37E-11	0.92E-10	0.52E-01	0.23E+00
1.0	8.	0.00E+00	0.76E-01	0.16E-09	0.40E-08	0.53E-01	0.23E+00
1.0	7.	0.00E+00	0.78E-01	0.73E-08	0.18E-06	0.55E-01	0.24E+00
1.0	6.	0.30E-05	0.80E-01	0.33E-06	0.80E-05	0.56E-01	0.25E+00
1.0	5.	0.12E-03	0.81E-01	0.15E-04	0.34E-03	0.57E-01	0.25E+00
1.0	4.	0.39E-02	0.77E-01	0.53E-03	0.11E-01	0.55E-01	0.24E+00
1.0	3.	0.62E-01	0.62E-01	0.11E-01	0.19E+00	0.46E-01	0.19E+00
1.0	2.	0.28E+00	0.31E-01	0.77E-01	0.85E+00	0.26E-01	0.94E-01
1.0	1.	0.23E+00	0.32E-02	0.88E-01	0.71E+00	0.40E-02	0.98E-02

Table 3—Continued

Time Gyr	R kpc	SFR(disk) $M_{\odot}yr^{-1}$	SFR(halo) $M_{\odot}yr^{-1}$	SN-Ia (disk) $100yr^{-1}$	SN-II (disk) $100yr^{-1}$	SN-Ia (halo) $100yr^{-1}$	SN-II(halo) $100yr^{-1}$
...
12.0	10.	0.00E+00	0.59E-01	0.13E-06	0.37E-06	0.14E+00	0.18E+00
12.0	9.	0.40E-05	0.60E-01	0.45E-05	0.12E-04	0.14E+00	0.18E+00
12.0	8.	0.10E-03	0.61E-01	0.12E-03	0.31E-03	0.15E+00	0.19E+00
12.0	7.	0.14E-02	0.62E-01	0.20E-02	0.43E-02	0.15E+00	0.19E+00
12.0	6.	0.87E-02	0.61E-01	0.16E-01	0.27E-01	0.15E+00	0.19E+00
12.0	5.	0.32E-01	0.56E-01	0.67E-01	0.99E-01	0.14E+00	0.17E+00
12.0	4.	0.83E-01	0.40E-01	0.19E+00	0.25E+00	0.11E+00	0.12E+00
12.0	3.	0.13E+00	0.14E-01	0.35E+00	0.40E+00	0.48E-01	0.43E-01
12.0	2.	0.63E-01	0.52E-03	0.24E+00	0.19E+00	0.56E-02	0.16E-02
12.0	1.	0.73E-02	0.00E+00	0.42E-01	0.22E-01	0.19E-03	0.99E-07
12.5	10.	0.00E+00	0.59E-01	0.16E-06	0.44E-06	0.14E+00	0.18E+00
12.5	9.	0.50E-05	0.59E-01	0.55E-05	0.14E-04	0.14E+00	0.18E+00
12.5	8.	0.12E-03	0.60E-01	0.15E-03	0.35E-03	0.15E+00	0.18E+00
12.5	7.	0.15E-02	0.61E-01	0.23E-02	0.46E-02	0.15E+00	0.19E+00
12.5	6.	0.89E-02	0.60E-01	0.16E-01	0.27E-01	0.15E+00	0.18E+00
12.5	5.	0.32E-01	0.55E-01	0.69E-01	0.99E-01	0.14E+00	0.17E+00
12.5	4.	0.82E-01	0.39E-01	0.19E+00	0.25E+00	0.11E+00	0.12E+00
12.5	3.	0.13E+00	0.13E-01	0.34E+00	0.38E+00	0.45E-01	0.40E-01
12.5	2.	0.58E-01	0.44E-03	0.23E+00	0.18E+00	0.50E-02	0.13E-02
12.5	1.	0.68E-02	0.00E+00	0.38E-01	0.21E-01	0.17E-03	0.70E-07
13.0	10.	0.00E+00	0.58E-01	0.20E-06	0.53E-06	0.14E+00	0.18E+00
13.0	9.	0.60E-05	0.59E-01	0.66E-05	0.17E-04	0.14E+00	0.18E+00
13.0	8.	0.13E-03	0.60E-01	0.17E-03	0.40E-03	0.15E+00	0.18E+00
13.0	7.	0.16E-02	0.60E-01	0.25E-02	0.49E-02	0.15E+00	0.19E+00
13.0	6.	0.92E-02	0.60E-01	0.17E-01	0.28E-01	0.15E+00	0.18E+00
13.0	5.	0.32E-01	0.54E-01	0.70E-01	0.99E-01	0.14E+00	0.17E+00
13.0	4.	0.81E-01	0.38E-01	0.19E+00	0.25E+00	0.10E+00	0.12E+00
13.0	3.	0.12E+00	0.12E-01	0.33E+00	0.37E+00	0.43E-01	0.38E-01
13.0	2.	0.54E-01	0.37E-03	0.21E+00	0.16E+00	0.44E-02	0.11E-02

Table 3—Continued

Time Gyr	R kpc	SFR(disk) $M_{\odot}yr^{-1}$	SFR(halo) $M_{\odot}yr^{-1}$	SN-Ia (disk) $100yr^{-1}$	SN-II (disk) $100yr^{-1}$	SN-Ia (halo) $100yr^{-1}$	SN-II(halo) $100yr^{-1}$
13.0	1.	0.64E-02	0.00E+00	0.35E-01	0.20E-01	0.16E-03	0.52E-07

Table 4. Model Results: Elemental Abundances.

Time	R	H	D	³ He	⁴ He	¹² C	¹³ C	¹⁴ N	O	Ne	Mg	Si	S	Ca	Fe
0.0	10.	0.770	0.70E-04	0.10E-04	0.230	0.10E-09	0.10E-09	0.10E-09	0.10E-09	0.10E-09	0.10E-09	0.10E-09	0.10E-09	0.10E-09	0.10E-09
0.0	9.	0.770	0.70E-04	0.10E-04	0.230	0.10E-09	0.10E-09	0.10E-09	0.10E-09	0.10E-09	0.10E-09	0.10E-09	0.10E-09	0.10E-09	0.10E-09
0.0	8.	0.770	0.70E-04	0.10E-04	0.230	0.10E-09	0.10E-09	0.10E-09	0.10E-09	0.10E-09	0.10E-09	0.10E-09	0.10E-09	0.10E-09	0.10E-09
0.0	7.	0.770	0.70E-04	0.10E-04	0.230	0.10E-09	0.10E-09	0.10E-09	0.10E-09	0.10E-09	0.10E-09	0.10E-09	0.10E-09	0.10E-09	0.10E-09
0.0	6.	0.770	0.70E-04	0.10E-04	0.230	0.10E-09	0.10E-09	0.10E-09	0.10E-09	0.10E-09	0.10E-09	0.10E-09	0.10E-09	0.10E-09	0.10E-09
0.0	5.	0.770	0.70E-04	0.10E-04	0.230	0.10E-09	0.10E-09	0.10E-09	0.10E-09	0.10E-09	0.10E-09	0.10E-09	0.10E-09	0.10E-09	0.10E-09
0.0	4.	0.770	0.70E-04	0.10E-04	0.230	0.10E-09	0.10E-09	0.10E-09	0.10E-09	0.10E-09	0.10E-09	0.10E-09	0.10E-09	0.10E-09	0.10E-09
0.0	3.	0.770	0.70E-04	0.10E-04	0.230	0.10E-09	0.10E-09	0.10E-09	0.10E-09	0.10E-09	0.10E-09	0.10E-09	0.10E-09	0.10E-09	0.10E-09
0.0	2.	0.770	0.70E-04	0.10E-04	0.230	0.10E-09	0.10E-09	0.10E-09	0.10E-09	0.10E-09	0.10E-09	0.10E-09	0.10E-09	0.10E-09	0.10E-09
0.0	1.	0.770	0.70E-04	0.10E-04	0.230	0.10E-09	0.10E-09	0.10E-09	0.10E-09	0.10E-09	0.10E-09	0.10E-09	0.10E-09	0.10E-09	0.10E-09
0.5	10.	0.770	0.70E-04	0.10E-04	0.230	0.59E-05	0.67E-07	0.14E-05	0.20E-04	0.40E-05	0.61E-06	0.65E-06	0.35E-06	0.52E-07	0.61E-06
0.5	9.	0.770	0.70E-04	0.10E-04	0.230	0.60E-05	0.69E-07	0.14E-05	0.21E-04	0.41E-05	0.62E-06	0.66E-06	0.35E-06	0.53E-07	0.62E-06
0.5	8.	0.770	0.70E-04	0.10E-04	0.230	0.62E-05	0.71E-07	0.15E-05	0.21E-04	0.42E-05	0.64E-06	0.68E-06	0.36E-06	0.55E-07	0.64E-06
0.5	7.	0.770	0.70E-04	0.10E-04	0.230	0.64E-05	0.74E-07	0.15E-05	0.22E-04	0.43E-05	0.66E-06	0.71E-06	0.38E-06	0.57E-07	0.66E-06
0.5	6.	0.770	0.70E-04	0.10E-04	0.230	0.67E-05	0.77E-07	0.16E-05	0.23E-04	0.46E-05	0.70E-06	0.74E-06	0.40E-06	0.60E-07	0.70E-06
0.5	5.	0.770	0.70E-04	0.10E-04	0.230	0.71E-05	0.82E-07	0.17E-05	0.25E-04	0.48E-05	0.74E-06	0.79E-06	0.42E-06	0.63E-07	0.74E-06
0.5	4.	0.770	0.70E-04	0.10E-04	0.230	0.77E-05	0.89E-07	0.19E-05	0.27E-04	0.53E-05	0.81E-06	0.86E-06	0.46E-06	0.69E-07	0.80E-06
0.5	3.	0.770	0.70E-04	0.10E-04	0.230	0.11E-04	0.12E-06	0.27E-05	0.42E-04	0.83E-05	0.13E-05	0.13E-05	0.69E-06	0.10E-06	0.11E-05
0.5	2.	0.769	0.70E-04	0.10E-04	0.230	0.36E-04	0.38E-06	0.92E-05	0.15E-03	0.30E-04	0.45E-05	0.46E-05	0.24E-05	0.35E-06	0.32E-05
0.5	1.	0.768	0.69E-04	0.10E-04	0.231	0.95E-04	0.10E-05	0.24E-04	0.38E-03	0.75E-04	0.11E-04	0.12E-04	0.61E-05	0.89E-06	0.85E-05
1.0	10.	0.770	0.70E-04	0.10E-04	0.230	0.14E-04	0.17E-06	0.32E-05	0.41E-04	0.81E-05	0.13E-05	0.15E-05	0.80E-06	0.13E-06	0.20E-05
1.0	9.	0.770	0.70E-04	0.10E-04	0.230	0.15E-04	0.17E-06	0.32E-05	0.42E-04	0.82E-05	0.13E-05	0.15E-05	0.82E-06	0.13E-06	0.20E-05
1.0	8.	0.770	0.70E-04	0.10E-04	0.230	0.15E-04	0.18E-06	0.33E-05	0.43E-04	0.84E-05	0.13E-05	0.15E-05	0.84E-06	0.13E-06	0.21E-05
1.0	7.	0.770	0.70E-04	0.10E-04	0.230	0.16E-04	0.18E-06	0.35E-05	0.45E-04	0.88E-05	0.14E-05	0.16E-05	0.87E-06	0.14E-06	0.22E-05
1.0	6.	0.770	0.70E-04	0.10E-04	0.230	0.16E-04	0.19E-06	0.36E-05	0.47E-04	0.92E-05	0.14E-05	0.17E-05	0.92E-06	0.15E-06	0.23E-05
1.0	5.	0.770	0.70E-04	0.10E-04	0.230	0.18E-04	0.21E-06	0.40E-05	0.52E-04	0.10E-04	0.16E-05	0.18E-05	0.10E-05	0.16E-06	0.24E-05
1.0	4.	0.770	0.70E-04	0.10E-04	0.230	0.25E-04	0.29E-06	0.58E-05	0.78E-04	0.15E-04	0.24E-05	0.27E-05	0.15E-05	0.23E-06	0.33E-05
1.0	3.	0.769	0.70E-04	0.10E-04	0.231	0.83E-04	0.96E-06	0.20E-04	0.27E-03	0.53E-04	0.82E-05	0.90E-05	0.48E-05	0.74E-06	0.97E-05
1.0	2.	0.765	0.68E-04	0.10E-04	0.233	0.30E-03	0.36E-05	0.73E-04	0.91E-03	0.18E-03	0.28E-04	0.31E-04	0.17E-04	0.26E-05	0.36E-04
1.0	1.	0.762	0.67E-04	0.10E-04	0.235	0.53E-03	0.67E-05	0.13E-03	0.15E-02	0.30E-03	0.46E-04	0.54E-04	0.30E-04	0.47E-05	0.72E-04
...
12.0	10.	0.767	0.68E-04	0.11E-04	0.232	0.21E-03	0.23E-05	0.42E-04	0.48E-03	0.92E-04	0.16E-04	0.30E-04	0.18E-04	0.34E-05	0.89E-04
12.0	9.	0.767	0.68E-04	0.11E-04	0.232	0.21E-03	0.24E-05	0.43E-04	0.49E-03	0.94E-04	0.16E-04	0.31E-04	0.18E-04	0.34E-05	0.91E-04
12.0	8.	0.767	0.68E-04	0.11E-04	0.232	0.24E-03	0.27E-05	0.50E-04	0.56E-03	0.11E-03	0.18E-04	0.35E-04	0.21E-04	0.38E-05	0.10E-03
12.0	7.	0.765	0.67E-04	0.12E-04	0.234	0.39E-03	0.46E-05	0.83E-04	0.93E-03	0.18E-03	0.30E-04	0.55E-04	0.33E-04	0.61E-05	0.16E-03
12.0	6.	0.759	0.63E-04	0.14E-04	0.237	0.83E-03	0.10E-04	0.19E-03	0.19E-02	0.37E-03	0.64E-04	0.12E-03	0.71E-04	0.13E-04	0.35E-03
12.0	5.	0.749	0.58E-04	0.18E-04	0.243	0.15E-02	0.20E-04	0.41E-03	0.34E-02	0.67E-03	0.12E-03	0.23E-03	0.14E-03	0.26E-04	0.70E-03

We now analyze the general results obtained with this bi-parametric grid of models, in particular the effect of the total mass and/or the morphological type on the rate of evolution. In order to do this, we represent them in four figures, Fig. 5, 6, 10 and 12, which we will analyze in the following subsections. In each one of them, we show 3 panels, corresponding to 3 different values of λ , i.e. different maximum rotation velocities and/or radial distribution of masses $M(R)$. We have selected the values corresponding to $\lambda = 0.03, 0.19$ and 1.0 , that means galaxies with rotation velocities of $48, 100$ and 200 kms^{-1} , respectively, as representing typical examples of spiral galaxies. For each panel we show the results for the 10 selected rates of evolution, or equivalently 10 morphological types from $T = 1$, the most evolved one, corresponding to the highest efficiency values ϵ_μ and ϵ_H , to $T = 10$, the least evolved.

3.1. Radial distributions of diffuse gas

The radial distribution of atomic gas surface density is shown in Fig. 5. We can see that the atomic gas surface density shows a maximum in somewhere along the disk, as it is usually observed. The central value of this maximum depends on Hubble type: the earlier type galaxies have smaller gas quantities and maximum values around $3\text{-}4 M_\odot/\text{pc}^2$. For intermediate types ($4 \leq T \leq 7$), these maximum values rise to $\sim 5 - 8 M_\odot/\text{pc}^2$. For all these morphological types the radial distributions are very similar independently of their galactic mass, except for those corresponding to $\lambda = 0.03$ ($V_{\text{rot}} = 48\text{kms}^{-1}$) which show much lower densities, except in the central region, for all morphological types.

The latest types ($T > 7$) display a clear dependence on galactic mass. The maximum density values are always large, due to the small efficiencies to form molecular clouds, which do not allow the consumption of the diffuse gas. But this density is $\sim 15 M_\odot/\text{pc}^2$ for $\lambda = 0.03$ ($V_{\text{rot}} = 48\text{kms}^{-1}$) and increases up to $\sim 30 - 40 M_\odot/\text{pc}^2$ for $\lambda = 1.5$ ($V_{\text{rot}} = 248\text{kms}^{-1}$).

In fact, a characteristic shown by all distributions is the similarity among models of the same morphological type but different total mass, when they are represented as a function of the normalized radius R/R_{opt} . With the exception of the $\lambda = 0.03$ model, all the others show, for the same T , differences small enough as to simulate a dispersion of the data.

The consequence of a shorter collapse time scale for the more massive spirals is clearly seen: the maximum is located at radii further away from the center due to the exhaustion of the diffuse gas in the inner disk which moves the star formation outside. The smaller the galaxy mass, the closer to the center is the maximum of the distribution, which resembles an exponential, except for the inner region. In fact, a shift in the maximum appears in each panel. In some cases, however, the low values of the surface gas density are due to the fact that the gas did not have enough time to fall completely onto the equatorial disk. This effect is very clear for the model with $\lambda = 0.03$ which shows a very steep distribution with densities lower than $15 M_\odot/\text{pc}^2$. In this case the gas shows a radial distribution with a maximum at the center.

Table 4—Continued

Time	R	H	D	³ He	⁴ He	¹² C	¹³ C	¹⁴ N	O	Ne	Mg	Si	S	Ca	Fe
12.0	4.	0.741	0.52E-04	0.23E-04	0.249	0.20E-02	0.32E-04	0.68E-03	0.47E-02	0.92E-03	0.16E-03	0.34E-03	0.21E-03	0.40E-04	0.11E-02
12.0	3.	0.735	0.48E-04	0.29E-04	0.252	0.24E-02	0.41E-04	0.91E-03	0.54E-02	0.11E-02	0.19E-03	0.44E-03	0.27E-03	0.52E-04	0.15E-02
12.0	2.	0.726	0.38E-04	0.49E-04	0.259	0.28E-02	0.58E-04	0.13E-02	0.63E-02	0.13E-02	0.24E-03	0.63E-03	0.39E-03	0.77E-04	0.23E-02
12.0	1.	0.703	0.16E-04	0.98E-04	0.274	0.39E-02	0.93E-04	0.21E-02	0.88E-02	0.18E-02	0.36E-03	0.11E-02	0.66E-03	0.13E-03	0.41E-02
12.5	10.	0.767	0.68E-04	0.11E-04	0.232	0.21E-03	0.24E-05	0.44E-04	0.50E-03	0.95E-04	0.16E-04	0.31E-04	0.19E-04	0.35E-05	0.94E-04
12.5	9.	0.767	0.68E-04	0.11E-04	0.232	0.22E-03	0.25E-05	0.45E-04	0.51E-03	0.98E-04	0.17E-04	0.32E-04	0.19E-04	0.36E-05	0.96E-04
12.5	8.	0.767	0.68E-04	0.11E-04	0.232	0.25E-03	0.29E-05	0.52E-04	0.59E-03	0.11E-03	0.19E-04	0.37E-04	0.22E-04	0.41E-05	0.11E-03
12.5	7.	0.764	0.67E-04	0.12E-04	0.234	0.42E-03	0.49E-05	0.90E-04	0.10E-02	0.19E-03	0.32E-04	0.60E-04	0.36E-04	0.66E-05	0.17E-03
12.5	6.	0.758	0.63E-04	0.14E-04	0.238	0.88E-03	0.11E-04	0.21E-03	0.21E-02	0.40E-03	0.68E-04	0.13E-03	0.76E-04	0.14E-04	0.38E-03
12.5	5.	0.748	0.57E-04	0.18E-04	0.244	0.15E-02	0.21E-04	0.43E-03	0.36E-02	0.70E-03	0.12E-03	0.24E-03	0.14E-03	0.27E-04	0.74E-03
12.5	4.	0.740	0.52E-04	0.24E-04	0.249	0.21E-02	0.33E-04	0.71E-03	0.48E-02	0.94E-03	0.17E-03	0.36E-03	0.21E-03	0.41E-04	0.11E-02
12.5	3.	0.735	0.48E-04	0.31E-04	0.253	0.24E-02	0.42E-04	0.93E-03	0.54E-02	0.11E-02	0.20E-03	0.45E-03	0.27E-03	0.53E-04	0.15E-02
12.5	2.	0.725	0.37E-04	0.53E-04	0.259	0.29E-02	0.59E-04	0.13E-02	0.64E-02	0.13E-02	0.25E-03	0.65E-03	0.40E-03	0.80E-04	0.24E-02
12.5	1.	0.702	0.14E-04	0.10E-03	0.275	0.40E-02	0.95E-04	0.21E-02	0.89E-02	0.18E-02	0.37E-03	0.11E-02	0.67E-03	0.13E-03	0.42E-02
13.0	10.	0.767	0.68E-04	0.11E-04	0.232	0.22E-03	0.25E-05	0.46E-04	0.52E-03	0.99E-04	0.17E-04	0.33E-04	0.20E-04	0.37E-05	0.98E-04
13.0	9.	0.767	0.68E-04	0.11E-04	0.232	0.23E-03	0.26E-05	0.47E-04	0.53E-03	0.10E-03	0.18E-04	0.34E-04	0.20E-04	0.38E-05	0.10E-03
13.0	8.	0.766	0.68E-04	0.11E-04	0.232	0.27E-03	0.31E-05	0.55E-04	0.63E-03	0.12E-03	0.20E-04	0.39E-04	0.23E-04	0.43E-05	0.11E-03
13.0	7.	0.764	0.66E-04	0.12E-04	0.234	0.45E-03	0.53E-05	0.97E-04	0.11E-02	0.20E-03	0.35E-04	0.65E-04	0.38E-04	0.71E-05	0.19E-03
13.0	6.	0.757	0.62E-04	0.14E-04	0.238	0.94E-03	0.12E-04	0.22E-03	0.22E-02	0.42E-03	0.72E-04	0.14E-03	0.82E-04	0.15E-04	0.41E-03
13.0	5.	0.748	0.56E-04	0.19E-04	0.245	0.16E-02	0.22E-04	0.46E-03	0.37E-02	0.72E-03	0.13E-03	0.25E-03	0.15E-03	0.29E-04	0.78E-03
13.0	4.	0.740	0.51E-04	0.24E-04	0.250	0.21E-02	0.34E-04	0.73E-03	0.49E-02	0.96E-03	0.17E-03	0.37E-03	0.22E-03	0.42E-04	0.12E-02
13.0	3.	0.734	0.47E-04	0.32E-04	0.253	0.24E-02	0.43E-04	0.95E-03	0.55E-02	0.11E-02	0.20E-03	0.46E-03	0.28E-03	0.54E-04	0.16E-02
13.0	2.	0.724	0.36E-04	0.56E-04	0.260	0.29E-02	0.61E-04	0.14E-02	0.65E-02	0.13E-02	0.25E-03	0.67E-03	0.41E-03	0.82E-04	0.25E-02
13.0	1.	0.700	0.13E-04	0.11E-03	0.276	0.40E-02	0.97E-04	0.22E-02	0.89E-02	0.18E-02	0.37E-03	0.11E-02	0.68E-03	0.14E-03	0.42E-02

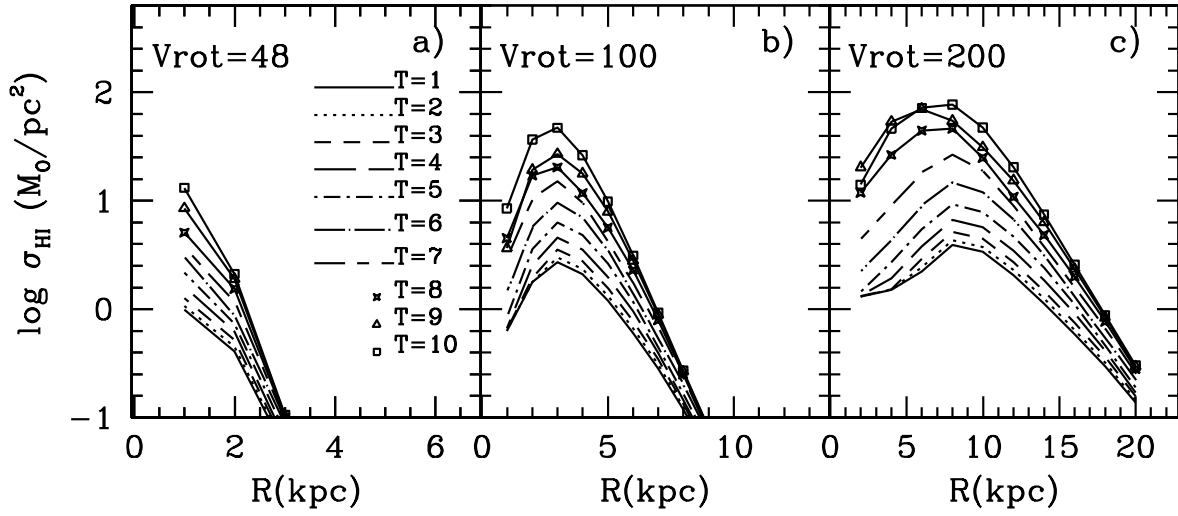


Fig. 5.— Present epoch radial distributions of the logarithmic surface density of the atomic gas for 3 different mass distributions following the V_{rot} 's values from each panel. In each one of them 10 morphological types are represented following labels in panel a).

Therefore, besides the variations due to the differences in total mass, which correspond to different collapse time-scales, a same total mass may produce disks in different evolutionary states. Thus, a same $\lambda = 0.15$ may result in a disk of 7-8 kpc and atomic gas densities around $5 M_{\odot}/pc^2$, or a disk of only 5 kpc with a maximum density of $40 M_{\odot}/pc^2$ in the region of 2 kpc. On the other hand, a galaxy with a large value of the total mass, may show a high gas mass density, and a little disk or on the contrary, be very evolved and therefore show no gas and a large stellar disk. The first object could correspond to the low surface brightness galaxies, while the last ones could be identified as the typical high surface brightness spiral galaxies.

3.2. Molecular gas radial distributions

An important success of the multiphase models has been the ability to reproduce the radial distributions for the atomic gas and the molecular gas separately, which is possible due to the assumed star formation prescription in two steps, allowing the formation of molecular clouds prior to the appearance of stars. Since the gas density in the disk depends only on the gravitational potential, and the cloud formation rate depends both on the efficiency to form clouds and the diffuse gas density, the molecular cloud density varies with the gravitational potential, and also with the index T .

Another important consequence of this SFR law is that it takes into account feedback mechanisms, even negative. If molecular clouds form before stars, this implies a delay in the time of star formation. The massive stars formed induce, in turn, the creation of new stars. But, at the same time these star formation processes also may destroy the diffuse or molecular clouds, by preventing the total conversion of the gas into stars and ejecting more gas once again into the ISM. In particular, massive stars destroy the molecular clouds that surround them, as Parravano (1990) explained, due to the sensitivity of molecular cloud condensation to the UV radiation. This mechanism restores gas to the ISM, thus decreasing the star formation. Both regulating process are included in our model. Neither heating or cooling mechanisms for the cloud components are included in our code.

The molecular gas shows an evolution similar to that of the diffuse gas, but with a certain delay. This delay allows the existence of an exponential function for a longer time, although in some evolved galaxies H_2 is also consumed in the most central regions, thus reproducing the so-called central *hole* of the molecular gas radial distribution. This is seen in Fig.6 for morphological types earlier than $T = 5, 6$ or 7 (depending on the total mass), for which the model lines turn over at the inner disk, which corresponds to the regions located at the border between bulge and disk. Thus, the more evolved galaxies show a maximum in their radial distribution of H_2 , which is always closer to the center than that of the atomic gas distribution.

The total quantity of gas in molecular form depends on two process: the creation of molecular clouds, (that depends on the diffuse gas mass available) and the process of conversion of the

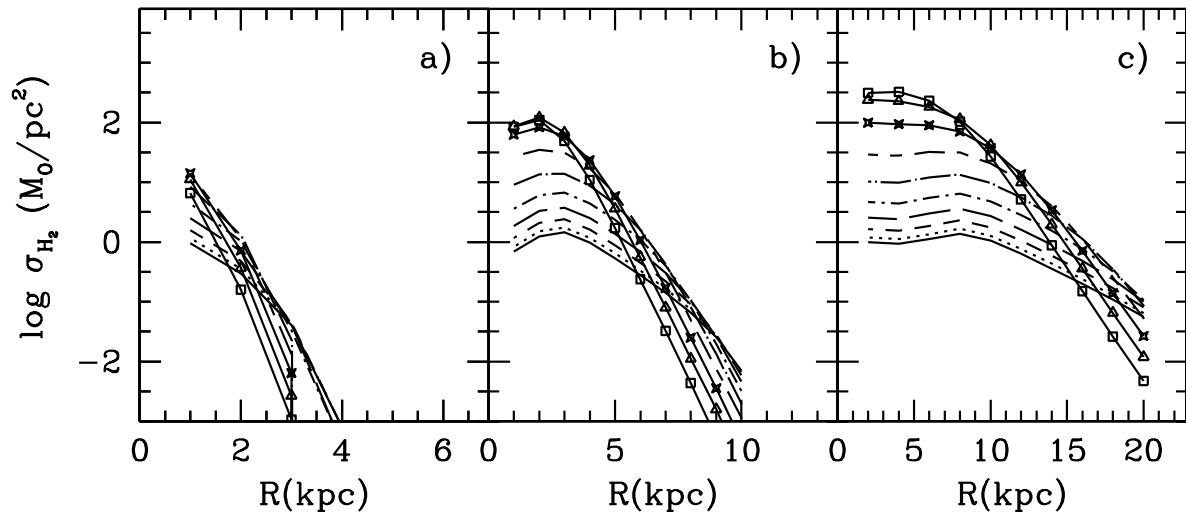


Fig. 6.— Same as Fig.5 for the molecular gas surface densities. Symbols are the same than in that figure.

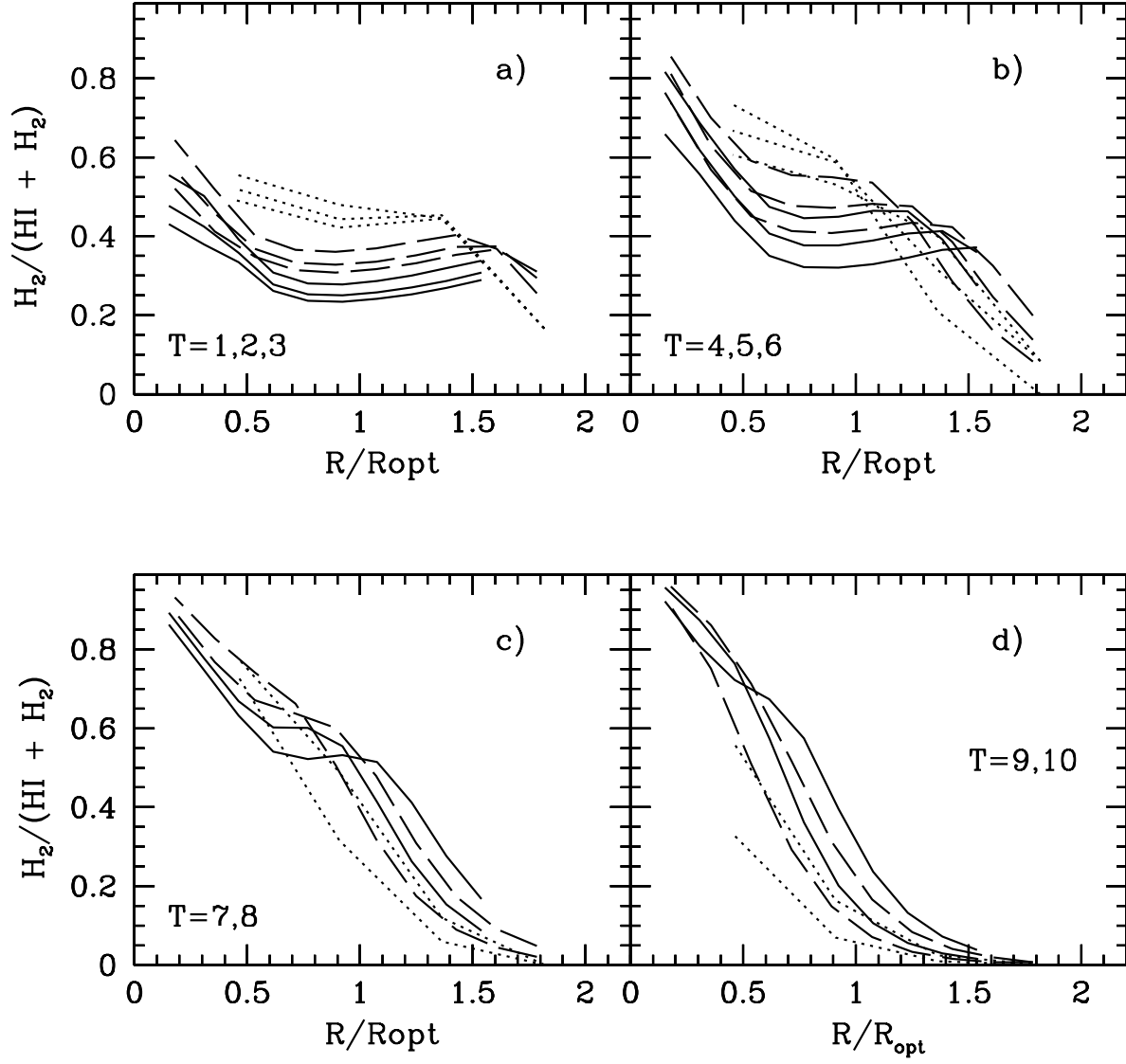


Fig. 7.— Present epoch radial distributions of the H_2/M_{gas} ratio for 3 different mass distributions in each panel. Labels have the same meaning than in Fig. 1

clouds into stars. Both effects have different rates for different type T. Therefore large quantities of molecular gas are only found in intermediate type galaxies: the earliest ones consume the molecular gas very quickly, by decreasing the surface densities to values smaller than $6 M_{\odot}/pc^2$, as observed in NGC 224, while the latest ones present rather long time scale to create clouds, due to the low efficiencies and to the low amount of diffuse gas available. This effect implies that the radial distributions do not have a continuous behavior with T: for T= 10, the radial distributions are, for some total masses, below those corresponding to earlier morphological types, as T= 7, 8, or 9. This effect is shown in Fig. 7, where we show, for each morphological type, the distributions of the ratio of molecular to total mass gas H_2/M_{gas} vs normalized radius R/R_{opt} . In each panel we show results for the different total mass values used in previous figures. We put together the same morphological type models giving similar distributions. Thus we see that there are 4 kind of behavior: The most evolved (T= 1to3) models have ratios as low as ~ 0.3 for all radial regions. For types 4 to 6 there exist models with a central maximum and some others with this maximum located out the central region. For types 7 and 8, the radial distributions show high values for the ratio H_2/M_{gas} for whole the disk, while for T= 10 the ratio is small except for the center where this is very high, almost 1.

Late-type galaxies show larger surface densities of molecular than atomic gas because the efficiency to form stars from molecular clouds is smaller than the efficiency to form these clouds. That is, the conversion of diffuse to molecular gas occurs more rapidly than the subsequent formation of stars. Thus these models predict larger quantities of molecular gas for the less evolved galaxies.

3.3. The radial stellar disks profiles

The total mass converted into stars form out the stellar disk in each galaxy. These stellar disks are reproduced in Fig.8 where we show in each panel the corresponding stellar surface density radial distributions for a given radial distribution of total mass.

In this case the morphological type has less influence in the resulting shape: the total mass of stars created is similar for all types $T < 6$, although they are formed at different rates, that is the resulting stellar populations have different mean ages. In the earliest types, stars were created very rapidly, while in the latest types, they formed later. Therefore the radial distributions of surface brightness results very similar for galaxies of all morphological types for a given galactic total mass, but colors are expected to be different, redder for the earlier type galaxies.

A very interesting result is that the central value is practically the same, around $100 M_{\odot}/pc^2$, for all rotation curves and morphological types in agreement with Freeman’s law. Only the less evolved galaxies or the less massive disks show central densities smaller than this value. We cannot compute a surface brightness only with these models, but assuming a ratio $M/L = 1$ for the stellar populations, this implies a surface luminosity density of $100 L_{\odot}/pc^2$ and scale lengths in agreement with observed generic trends. In any case, all information related to photometric quantities, and

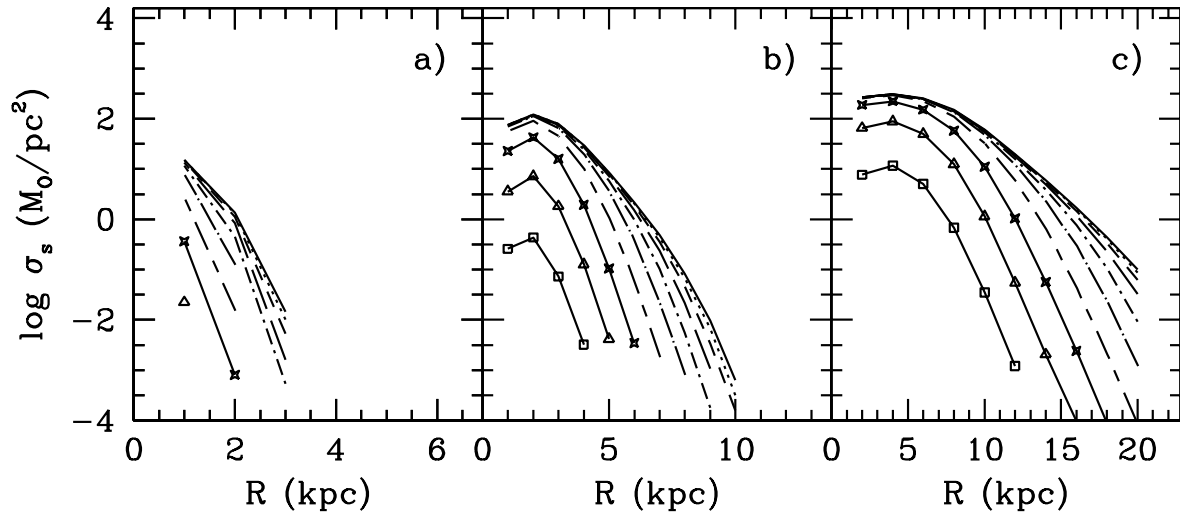


Fig. 8.— Present epoch radial distributions of total mass surface density for 6 different mass distributions. Ten different morphological type are shown in each panel. Symbols are the same than in Fig.5.

this also applies to the disk scale lengths, must be computed through the application of evolutionary synthesis models. These must be calculated from the star formation histories resulting from the chemical evolution models shown here, but this is out of the scope of this work and will be addressed in a forthcoming work.

Only in models with $T > 7$ the stellar disks show a different appearance: they look less massive, as corresponding to disks in the process of formation. This implies that the surface brightness is lower than for the other types for a similar characteristic total mass in the protogalaxy.

In this way, we can reproduce the characteristics observed by de Blok & McGaugh (1996) who show how two galaxies with very similar rotation curves may, however, have very different radial distributions of gas and stars. In Fig.9 we represent the radial distribution of stars, gas and gas plus stars predicted by 2 models computed with the same radial distribution of total mass and different efficiencies corresponding to morphological types 5 and 7. The X-axis is taken as the measure of scale lengths obtained from the corresponding stellar radial distribution shown in Fig. 8. The first model, $T = 7$, has a large amount of gas, still not consumed, and its stellar profile differs strongly from that corresponding to its total mass. We can see, however, that the model for $T = 5$ shows a lower gas density for the whole disk than that for $T = 7$, due to its larger star formation efficiency. Its stellar component has a cutoff radius shorter than the gas but, except for this feature, it is very close to the total mass distribution. We must realize that the $T = 7$ model looks more extended than type 5. This effect is due to the representation on scale length units. Due to the steeper stellar profile for the later type, which only produces stars at the center of the disk, the scale length is smaller than that of the earlier type model, which has a flat stellar radial distribution. Therefore, more scale lengths are needed to represent the whole galaxy. Nevertheless, the comparison of our Fig.9 with Fig.2. from de Blok & McGaugh (1996) shows that it is extremely similar, thus proving that galaxies found to have the same mass and different surface brightness may also be explained with our models as resulting from different cloud and star formation rates or different efficiencies. These efficiencies include the dynamical information not treated explicitly in our models, and therefore, the existence of two models with the same total mass and different surface brightness may only be explained by differences in the temperature and other thermodynamical conditions, which would not depend on gravitational potential.

3.4. The elemental abundances

One of the most important results of this grid of models refers to the oxygen abundances, shown in Fig. 10. A radial gradient appears for most of models. This is due to the different evolutionary rates along radius: the inner regions evolve more rapidly than the outer ones, thus steepening the radial gradient very soon for most models. Then, the radial gradient flattens for the more massive and/or earlier galaxies due to the rapid evolution which produces a large quantity of elements, with the oxygen abundance reaching a saturation level. This level is found to be around $12 + \log(O/H) \sim 9.0 - 9.1$ dex. Observations in the inner disk of our Galaxy support this statement

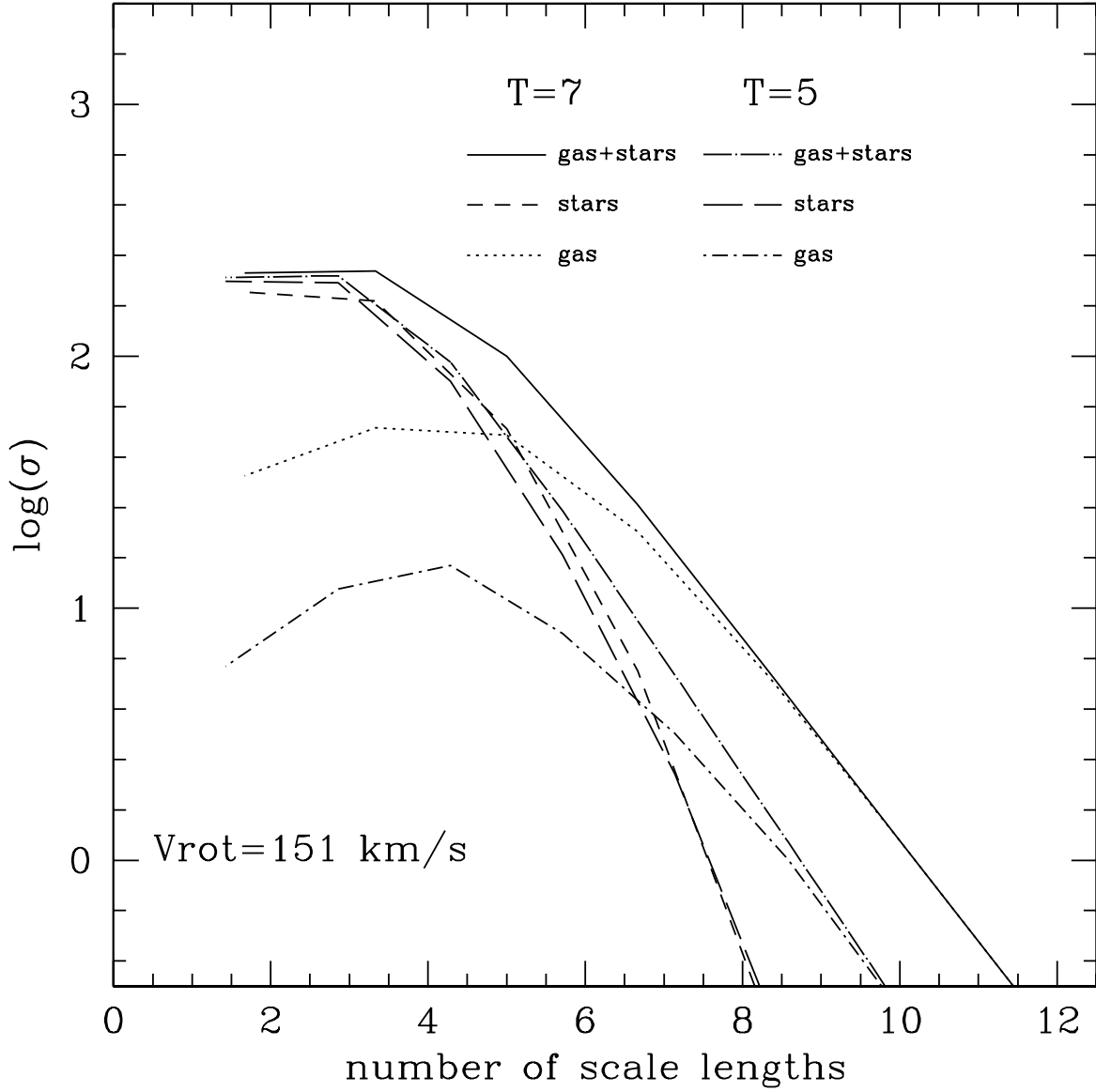


Fig. 9.— Present epoch radial distributions of stars, gas and gas plus stars, for 2 models with the same radial distribution of total mass, corresponding to $V_{rot} = 151 km s^{-1}$, and 2 different morphological types, T = 4 and T = 7.

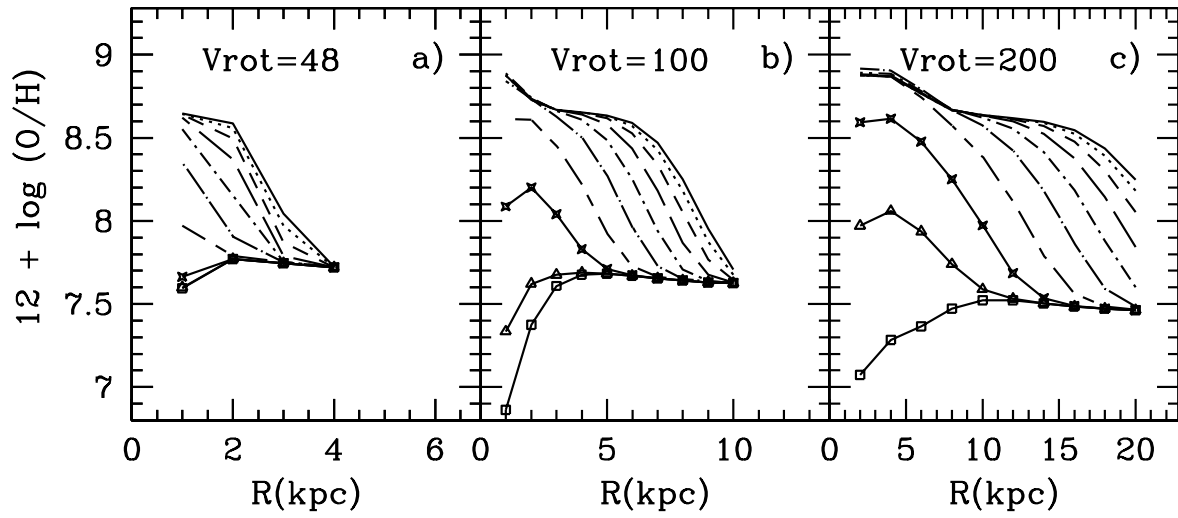


Fig. 10.— Present epoch radial distributions of Oxygen abundance, $12 + \log(O/H)$, for 3 different mass distributions. Ten different morphological type are shown in each panel. Symbols are the same than in Fig.5

(Smartt et al. 2001).

Moreover, the larger the mass of the galaxy, the faster the effect: a galaxy with $V_{rot} = 100 \text{ km s}^{-1}$ has a flat radial gradient for types $T = 1$ or 2 , while a galaxy with $V_{rot} = 200 \text{ km s}^{-1}$, shows a flat distribution for all types earlier than 4 . The less massive galaxies maintain a steeper radial distribution of oxygen for almost all types, with very similar values for the gradients. Our models reproduce very well the observed trend: the later the type of a galaxy, the steeper its radial distribution of abundances.

Nevertheless, for any galaxy mass, *the latest types $T > 7 - 8$ show flat radial abundances distributions*. Thus, the late galaxies types show no gradient, the intermediate types show steep gradients, and the early galaxies have, once again, flat abundance radial distributions. The largest values of radial gradients correspond to the intermediate types of galaxies, with the limiting types varying according to the total mass of the galaxy. The more massive galaxies only show a significant radial gradient for $T = 8$ and 9 , while the less massive ones have a flat gradient only for $T = 9$ or 10 , the other types having very pronounced radial gradients even for $T = 1$.

In the early type galaxies, the characteristic efficiency ϵ_μ is high for all the disk, thus producing a high and early star formation in all radial regions. In this case, the oxygen abundance reaches very soon the saturation level or *effective yield*, flattening the radial gradient developed in the first times of the evolution. The characteristic oxygen abundance, measured at R_0 , is higher for the more massive galaxies and lower for the less massive ones. However, this correlation is not apparent when the central abundance is used, due to the existence of this saturation level in the oxygen abundance, which produces a flattening of the radial gradient in the inner disk, even for intermediate type galaxies.

In fact, the oxygen abundance radial distribution shows sometimes a bad fit to reported distributions in the central parts of the disks, which give frequently abundances larger than 9.10 dex. This absolute level of abundance is not reached in any case by the models. All the computations performed within the multiphase approach reach a maximum $12 + \log(O/H) \sim 9.10$ dex which no model can exceed. It should be recalled, however, that all oxygen data yielding values larger than 9.1 dex have been obtained in HII regions where the electronic temperature could not be measured, and abundances have been estimated through empirical calibrations which are very uncertain in the high abundance regime. In fact, the shape of the radial distribution of oxygen changes depending on the calibration used to estimate them (e.g. Kennicutt & Garnett 1996). The suspicion that these abundances are overestimated at least by a factor 0.2 dex is very reasonable (Pilyugin 2000, 2001; Díaz et al. 2000; Castellanos, Díaz, Terlevich 2002).

Therefore, the gradient behavior found in the models seems to be in agreement with observations solving the apparent inconsistency in the trends giving larger gradients for late types of galaxies and flatter ones for the earliest ones while some irregulars show no gradient at all, with very uniform abundances.

3.5. Relative Abundances

The relative abundances among elements give information about the scales of evolution in galaxies or regions where the star formation rates are different. When the high star formation rates produce very rapidly a large number of stars, the oxygen ejected mostly by the more massive stars appears in the interstellar medium at the first epoch of the evolution. The iron ejected by the low mass stars appears, at least, 1 Gyr later. If the star formation has ceased to create stars, due, for example, to the consumption of the gas, stars cannot incorporate this iron in their interiors. Thus the stellar abundance $[O/Fe]$ would have over-solar values. If the star formation produces stars at a lower rate, more continuously, they would be created with a similar abundance in oxygen and iron, and therefore the mean relative abundance will be around solar.

Our models produce a large number of stars when the morphological types are early or when the galaxies are massive, which implies higher infall rates and more rapid evolution in their disks. We can see this effect in Fig. 11 where we show in each panel the resulting $[O/Fe]$ vs $[Fe/H]$ for a given radial distribution of total mass and for the 10 morphological types. It is clear that all type of massive galaxies produce over-solar abundances $[O/Fe]$, with values $\sim 0.5 - 0.8$, for metallicities $[Fe/H] < -0.7$ dex. For the low mass galaxies this occurs only for the earliest morphological types, while the later ones have smaller values of $[O/Fe]$. For these latter galaxies, the $[O/Fe]$ ratio starts to decrease toward solar values at lower metallicities (~ 2.5 dex) than for the more massive galaxies, which maintain their iron underabundances until higher metallicities (~ -1.5 dex)

The usual *plateau* in the relation $[O/Fe]$ vs $[Fe/H]$, also found in our previous models, is steeper in this new work. The only possible explanation resides in the different nucleosynthesis yields for the massive stars used now in comparison to those used before: Woosley & Weaver (1995) yields produce more iron than the old yields (Woosley & Weaver 1986), and therefore the ratio $[O/Fe]$ decreases, although smoothly, from the beginning. When the SN-I's explosions start the iron increases suddenly and the slope of the relation steepens abruptly. The change of slope indicates the time when this occurs.

3.6. The star formation rate

Radial distributions of star formation rate surface density show an exponential shape in the outer disk, but a less clear one in the inner regions, where some models show a distribution flatter than the molecular gas, and even, decreasing toward low values of the star formation rate in the center. Although at first look the SFR radial distributions seem to be different from those obtained by Kennicutt from $H\alpha$ fluxes, the comparison of some particular models with galaxy data results acceptable, as we will see in Section 4.2.

This effect is due to the star formation law assumed in the multiphase model which has two modes to form stars: the spontaneous one, depending on radius through the efficiency to form

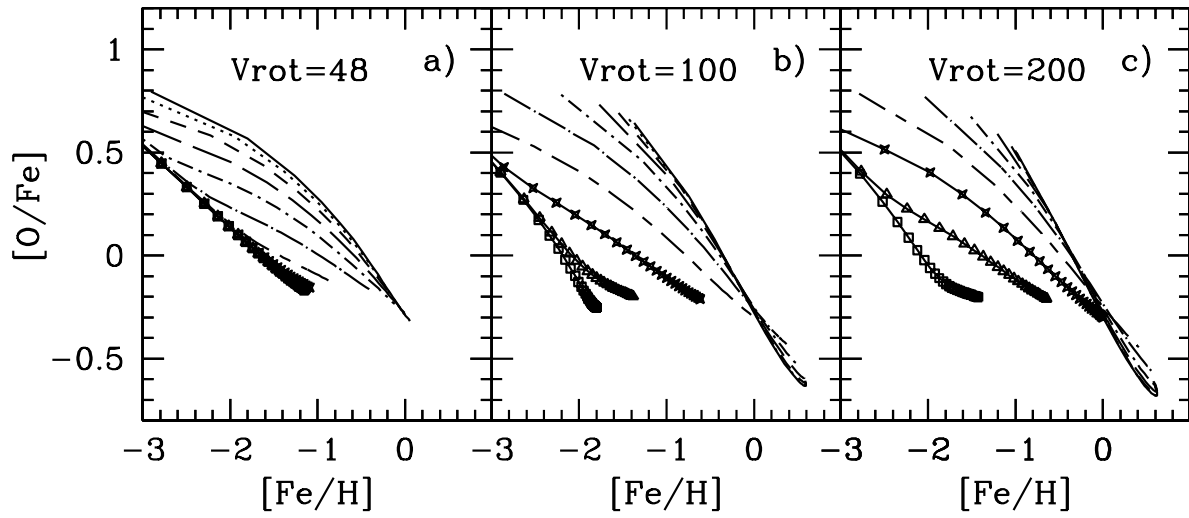


Fig. 11.— Relative abundances $[O/Fe]$ vs $[Fe/H]$ for 3 different mass distributions in each panel. Ten different morphological type are shown in each panel. Line types have the same meaning than in Fig. 5

molecular clouds, stronger in the inner than in the outer disk; the stimulated one, resulting from the interactions of molecular clouds with the existing massive stars. Thus, the star formation rate depends on the molecular gas surface density and also on the massive stars one.

This relation reproduces the Kennicutt’s relation (Kennicutt 1989), which has two slopes when the SFR is represented vs the total gas surface density, Fig. 13. This means that a threshold in the star formation is not strictly necessary since the same effect is obtained when molecular gas and self-regulation are considered.

The star formation rate assumed in our models do not produce bursts in the low mass galaxies of any morphological type. Only the massive galaxies are able to keep a large quantity of gas in a small region, usually at the centers although sometimes at the inner disk regions. On the contrary, low mass galaxies collapse very slowly, and thus the star formation rate maintains a low level during the whole life of the galaxy. In fact recent works suggest the same scenario for both low mass and low surface brightness galaxies (van den Hoek, van der Hulst, & de Jong 2000; Legrand 2000; Braun 2001) in order to take into account the observed data. Our resulting abundances and gas fractions are in agreement with these data, although the photometric observations cannot still be compared with the results of our model.

4. Analysis of model results: Tests

With the selection of parameters and inputs described above, we have ran a total of 440 models, with 44 different rotation curves –implying 44 values of total mass, characteristic collapse time scale and disk radius– and 10 morphological types for each one of them, implying 10 evolutionary rates for the star formation and gas consumption in the disk.

For each model we obtain the time evolution of the halo and the disk, and therefore the corresponding radial distributions for the relevant quantities (masses, abundances, star formation rate, etc...). The star formation history is followed for each radial region (halo and disk, separately) and within each one, the mass in each phase of matter: diffuse gas, molecular gas, low-mass stars, massive stars and remnants, is also followed. Besides that, we obtain abundances for 15 elements: H, D, He3, He4, C12, C13, N14, O16, Ne, Mg, Si, Ca, S, Fe and neutron-rich nuclei in all radial regions for both halo and disk.

We now will compare the results with observational data in order to see if models are adequately calibrated.

4.1. Application to the MWG

The first application of any theoretical model is to check its validity to the MWG. A large set of observational data for the Solar Neighborhood and the galactic disk exists and therefore the

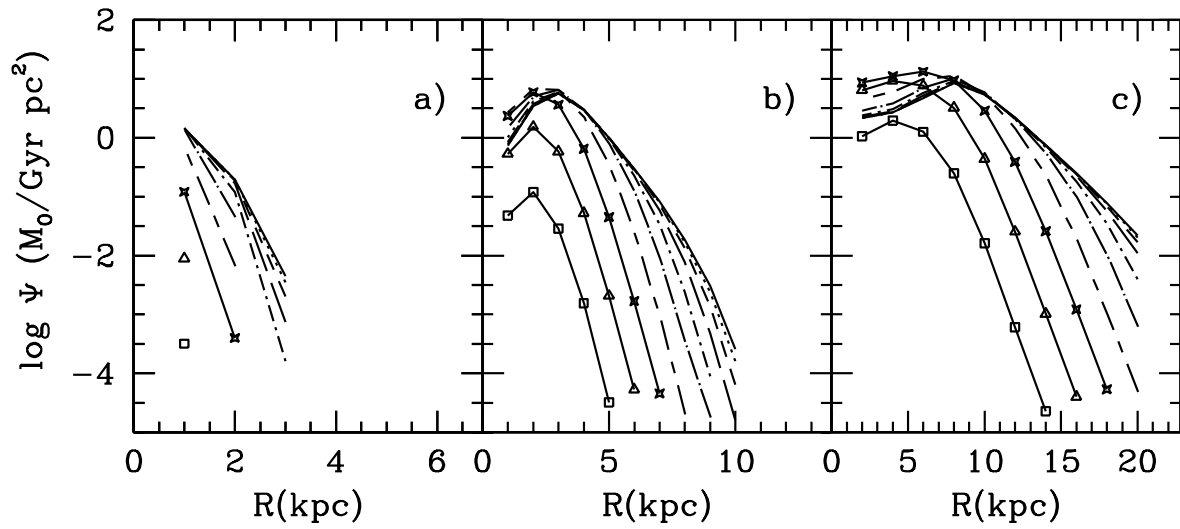


Fig. 12.— Present epoch radial distributions of the surface density of the star formation rate for 3 different mass distributions. Labels have the same meaning than in Fig.10

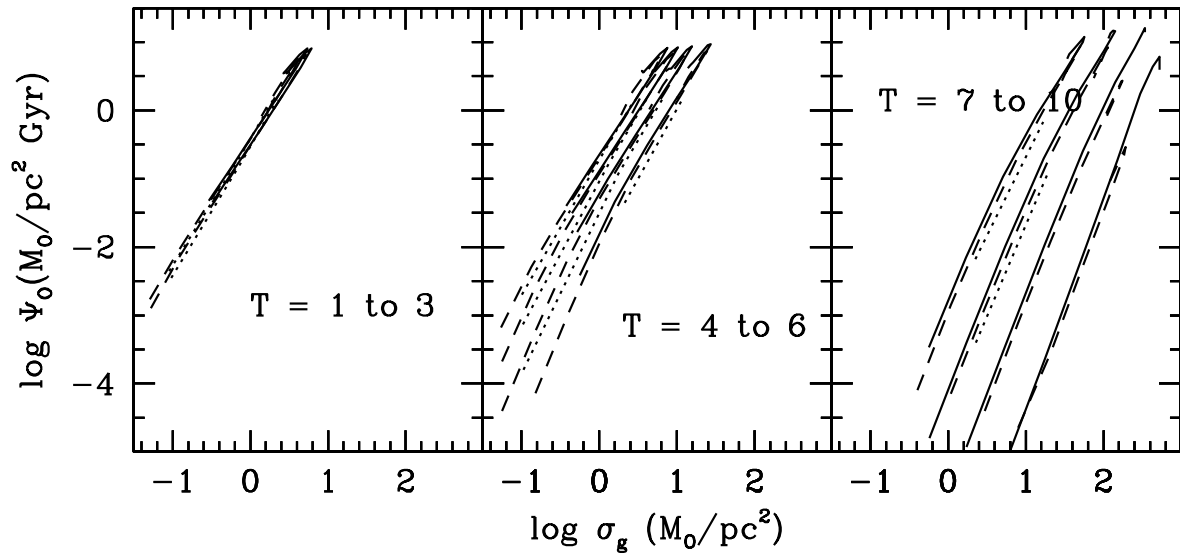


Fig. 13.— The relation of the surface density of the star formation rate with the total gas density for 3 different mass distributions and different morphological type as labeled

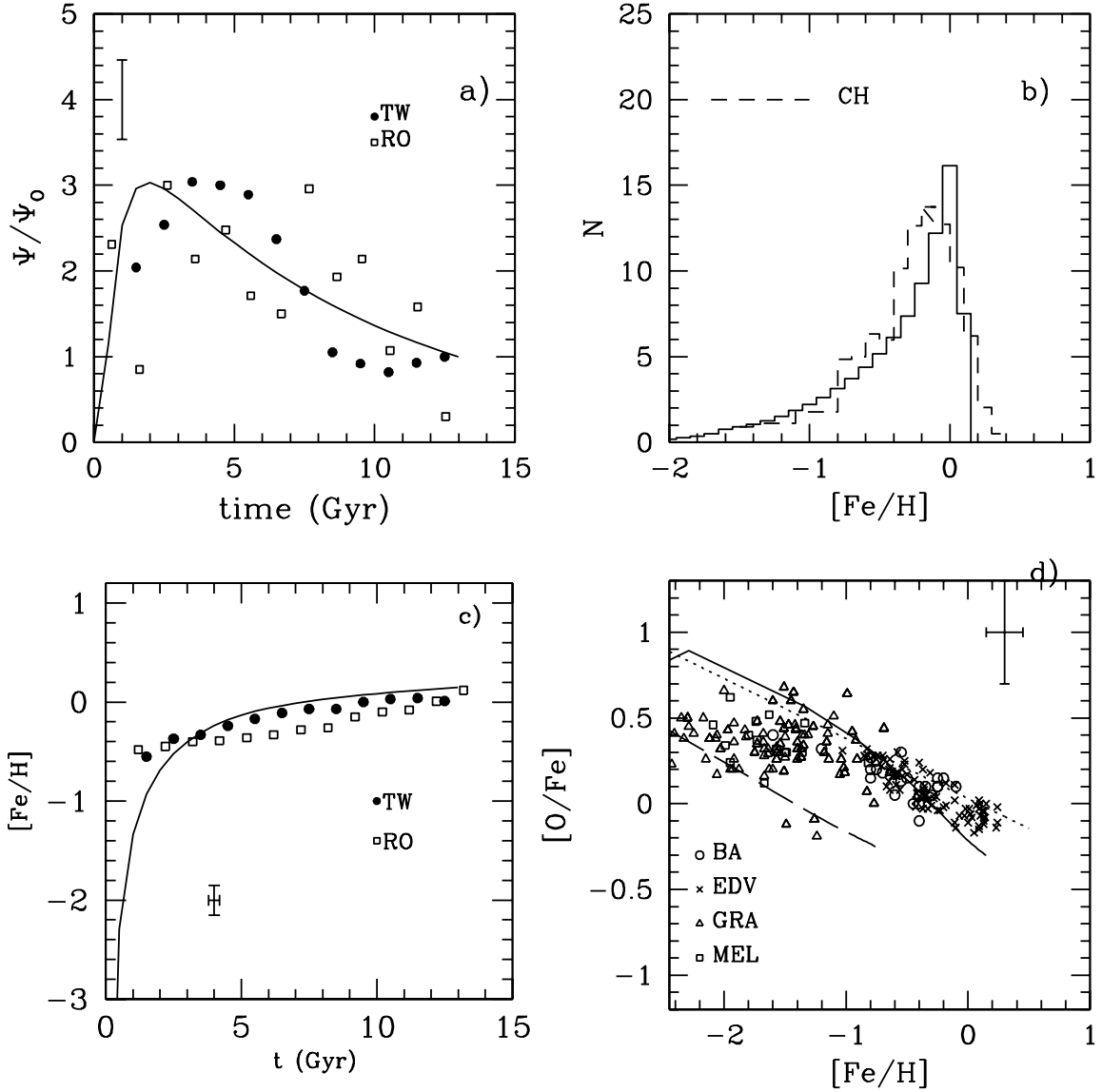


Fig. 14.— The Solar Neighborhood disk evolution as results from the chosen MWG model for the region located at $R = 8$ kpc. a) The star formation history with data from Twarog (1980) –filled dots:TW– and Rocha-Pinto et al. (2000b) –open squares: RO–; b) The metallicity distribution compared with the observed distribution from Chang et al. (1999); c) The age-metallicity relation with data from Twarog (1980) –filled dots:TW– and Rocha-Pinto et al. (2000a) –open squares: RO–; and d) the relation $[\text{O}/\text{Fe}]$ vs $[\text{Fe}/\text{H}]$ for the disk (solid line) and for the halo (long dashed line) region models with data Barbuy & Erdelyi-Mendes (1989) –open dots: BA–, Edvardsson et al. (1993) –crosses:EDV, Gratton et al. (2000) –open triangles: GRA–, and Meléndez, Barbuy, & Spite (2001) –open squares: MEL–. The dotted line is the mean relation given by Boesgaard et al. (1999).

number of constraints is large compared to the free parameters of the computed models.

The model for $T = 4$, and total mass distribution number 28, $\lambda = 1.0$ and maximum rotation velocity $V_{max} = 200 \text{ km s}^{-1}$, has been chosen for comparison with the MWG.

The results corresponding to this model are represented in Figs. 14 and 16 together with the available data. In Fig. 14 we show the results for the disk Solar Neighborhood, that is, the disk region located at $R=8$ kpc from the Galactic center. The left panels a) and c) show the star formation history and the age-metallicity relation. Both graphs reproduce adequately the observed trends, although the model predicted star formation maximum appears slightly shifted to earlier times with respect to observations, and the high iron abundances observed at times earlier than 1 Gyr are not fitted by the model.

Right panels b) and d) show the disk metallicity distribution and the $[\text{O}/\text{Fe}]$ vs $[\text{Fe}/\text{H}]$ relation. Both figures provide information about the scale of star formation and enrichment. They also show a reasonable agreement with available observational data. The metallicity distribution resulting of the model does not show the G-dwarf problem: as we can see, there is no excess of metal-poor stars.

In the last panel d) data refer to disk (open dots and crosses) and halo (triangle and squares) stars, while the solid line refers to the disk region model which falls on the disk data locus. The model also predicts higher values of O/Fe for low metallicities but, taking into account the stellar metallicity distribution, not many disk stars are expected in this location in the diagram.

The data corresponding to the halo stars show two different behaviors depending on how measurements are made. We have included the mean relation given by Boesgaard et al. (1999), –dotted line–, who gives a review discussion about the subject and recalculates some of these abundances, but these values are doubtful and under debate. The halo model (long dashed line) shows a lower value, around 0.5 dex, as shown by recent data from Gratton et al. (2000) and Meléndez, Barbuy, & Spite (2001). For larger metallicities this value decreases, but, as in the previous comparison, there are no many halo stars in this locus, as the star formation in the halo decreases very quickly after the first Gyr.

Our models do not cover the region where the highest metallicity halo stars lie. This is probably due to the fact that the thick disk is not considered as a separate component. In fact, there exists a continuous sequence of stellar populations along the vertical direction that would imply a continuous star formation and the existence of stars located between our two model (halo and disk) lines.

Our treatment allows star formation in the galaxy barionic halos which produces an certain level of enrichment. In the case of our galaxy, this enrichment is in agreement with data for the Solar Neighborhood halo. This is shown in Fig. 15 where we plot the evolution of the halo for the region located at $R= 8$ kpc, for the model representing the MWG. We can see that the age-metallicity relation of the halo reproduces the data from Schuster & Nissen (1989).

Moreover, the ratio $M_{\text{halo}}/M_{\text{disk}}$ must reproduce the value given by observations (Sandage

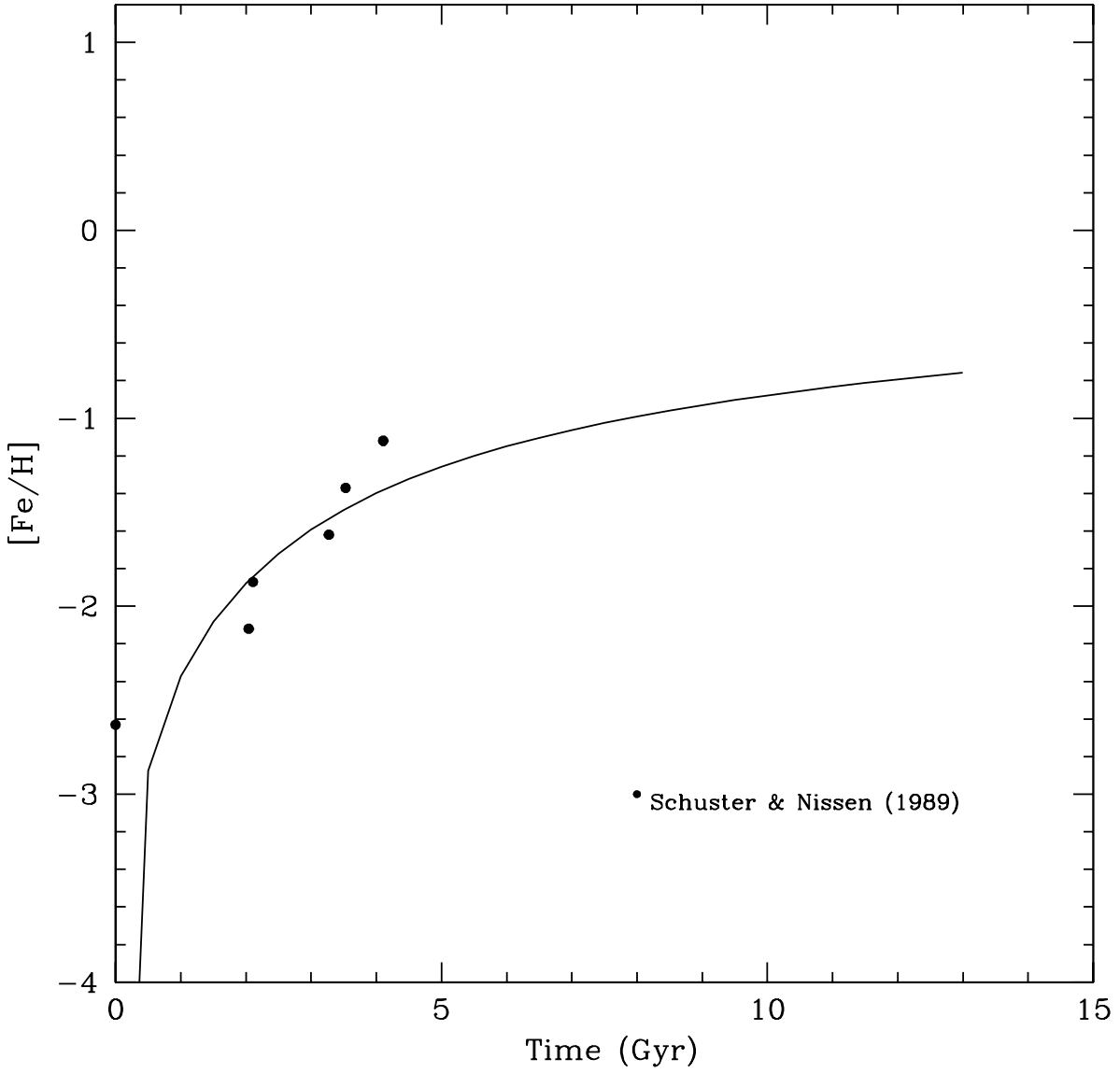


Fig. 15.— The Solar Neighborhood halo region evolution as results from the chosen MWG model for the halo region located at $R = 8$ kpc: The age-metallicity relation with data from Schuster & Nissen (1989) –filled dots:SN.

1987) as we have already explained in Section 2. Since we only deal with two components including the thick disk in the halo (or in the disk) region, the fraction $M_{\text{halo}}/M_{\text{disk}}$ must be around 0.10. In our model 28, $T=4$, for $R=8$ kpc, the halo to disk stellar mass ratio is around 1/9 in agreement with those estimates.

Fig. 16 shows the radial distributions of diffuse and molecular gas, stars, total mass, star formation rate and oxygen and nitrogen abundances for the galactic disk. The shape of the observed radial distribution is well reproduced for the diffuse gas, with a maximum in the outer disk. For the total mass it is an exponential distribution in agreement with the surface brightness distribution, and radial gradients of abundances similar to those shown by the most recent data.

For the molecular gas density is a quasi-exponential law, which decreases at the inner disk regions ($R \leq 7$ kpc). This decreasing may be eliminated if we assume a decreasing of the cloud-cloud collision process efficiency in those zones, but then the oxygen abundance would also decrease in the center of the disk, in disagreement with observations. On other hand it is necessary to remind that the molecular masses are estimated from the CO intensity through a calibration factor. This factor depends on metallicity (Verter & Hodge 1995; Wilson 1995) in a way which would produce smaller molecular gas densities at the inner galactic disk if it is used. By taking into account that recent data give low densities at these inner regions, we consider that our model results may represent adequately the reality.

The radial distributions for oxygen and nitrogen (and also for other element not shown here) show the usual variation with galactocentric radius with a radial gradient in the range of what it is observed. Although the fact of reproducing this characteristics cannot be considered as a positive discriminant, this must be nevertheless imperative for any one. We show that our model reproduces the data within the errors and dispersion range. On the other hand, this model shows a flattening in the inner disk which is in agreement with the recent observations from Smartt et al. (2001).

The only feature which is not well reproduced is the SFR that decreases toward the inner disk in apparent inconsistency with observations. The star formation rate has a maximum in $R \sim 7 - 8$ kpc, while the observed star formation rate radial distribution increases exponentially towards the center, or it has a maximum in 3-4 kpc. In fact, it results difficult to explain why the star formation rate is still so high at the inner disk, (in regions located at 3-4 kpc), where both phases of gas are already consumed. The maximum of the atomic gas density is around of 10-11 kpc, and the molecular gas density has its maximum around 6 kpc. Negative feedback caused by the increase of the cloud velocity dispersion might be an answer. This effect is not taken into account in our models and may delay the star formation in such way that the gas density remains high for a longer time which, in turn, would imply a stronger star formation rate at present. On the other hand, recent data on the radial distribution of OB star formation in the Galaxy (Bronfman et al. 2000) shows a maximum around 5 kpc, decreasing towards both sides. This may be an indication that the SFR indeed has a maximum along the galactic disk, although the detection of young sources, which are embedded in gas clouds, is difficult and might result in a selection effect. Nevertheless,

a decrease in the star formation radial distribution for the inner regions of disks is observed in a large number of galaxies, as we will see in the next section.

4.2. Individual galaxies

In what follows we analyze the radial distributions for gas, star formation and abundances for some galaxies with large observational data sets in order to check if the generic model reproduces the observed characteristics of particular galaxies.

The characteristics and corresponding input parameters of this representative galaxy sample are given in Table 5. For each galaxy, Column (1), the morphological type index is given in Column (2), while the classical Hubble type is given in Column (3). The adopted distance (taken from references following Table 6, Column 2) is in Column (4), the maximum rotation velocity is given in Column (5) and the characteristic radius in Column (6). The last columns, (7) to (9) give the collapse time scale and efficiencies for molecular cloud and star formation. The last column is the number of the radial distribution of total mass –corresponding to the column (1) of Table 1– chosen for each galaxy.

The radial distributions of the different quantities for these galaxies are shown in Fig. 17 together with the corresponding observational data, taken from references given in Table 6.

In the first row of panels of Fig. 17 we can clearly see that the radial distributions of neutral hydrogen are well reproduced by the models. We would like emphasize that, besides the fact that there are no models which try to reproduce the radial distribution of galaxies different than the ours, this comparison with diffuse gas data has not been performed by any chemical evolution model because, usually, the total gas, not the diffuse and molecular gas separately, is used for fitting models.

Table 5. Galaxy Sample Characteristics and Model Input Parameters.

Galaxy Name	T	Type Class	D (Mpc)	Vel _{rot,max} (kms ⁻¹)	R ₀ (kpc)	τ ₀ (Gyr)	ε _μ	ε _H	Mass Distr. Number
NGC 300	7	Scd/Sd	1.2	85	2.3	13.3	8.62E-02	2.18E-03	13
NGC 598	6	Sc/Scd	0.9	110	2.9	10.3	1.58E-02	1.11E-02	20
NGC 628	5	Sc	11.4	220	7.7	3.28	2.86E-01	4.39E-02	32
NGC 4535	5	—	16.8	210	7.4	3.50	2.86E-01	4.39E-02	31
NGC 6946	6	Scd	5.9	180	6.2	4.26	1.58E-02	1.11E-02	25

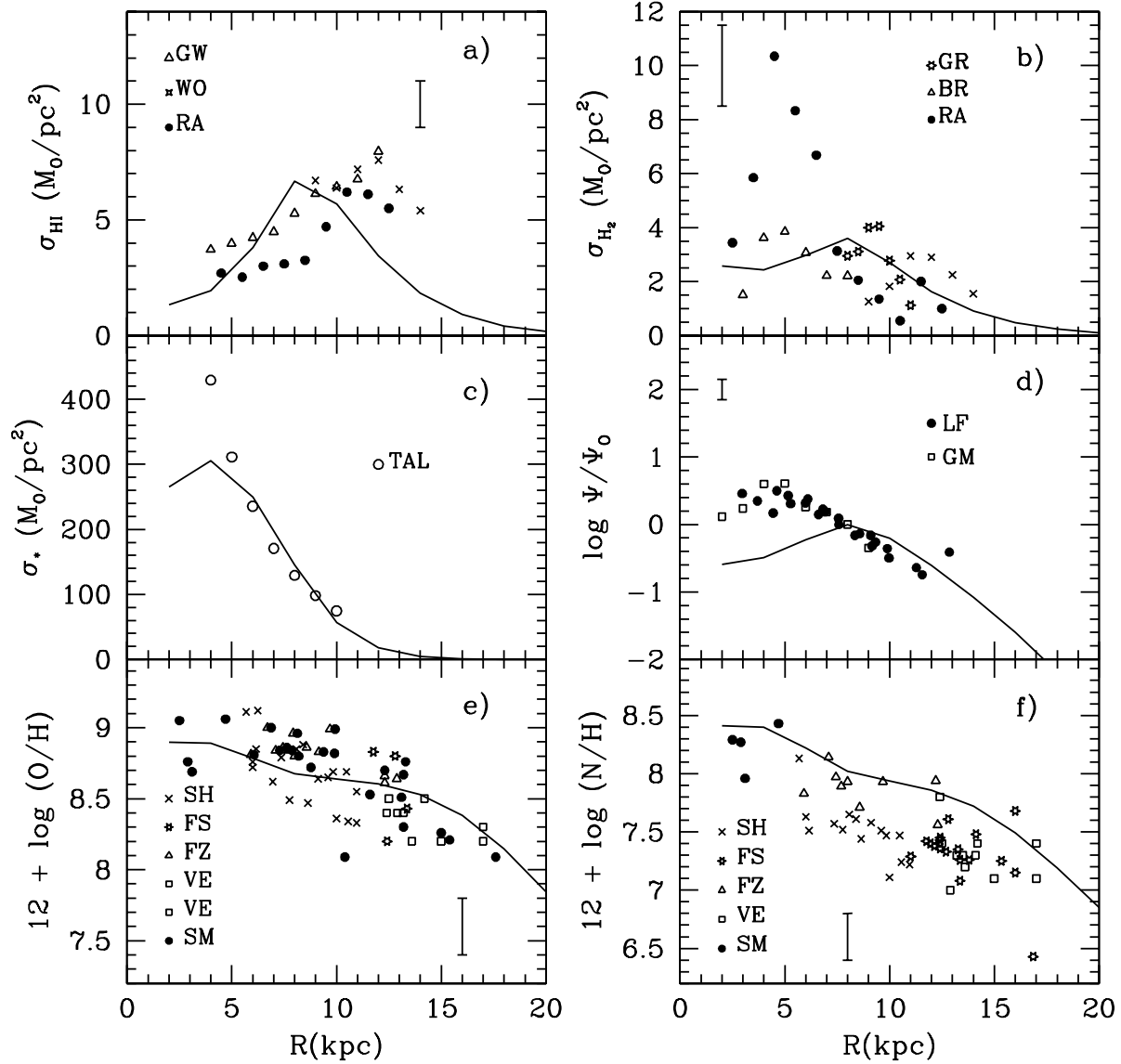


Fig. 16.— Present epoch radial distributions for the MWG simulated galaxy (distribution number 28, $\lambda = 1.00$, $T = 4$): a) atomic gas density with data from Garwood & Dickey (1989) –open triangles: GW–, Wouterlook et al. (1990) –crosses: WO–, and Rana (1991) –filled dots:RA–; b) molecular gas surface density with data from Grabelsky, Cohen & Bronfmann (1987) –stars: GR–, Bronfman et al. (1988) –open triangles:BR–, and Rana (1991) –filled dots: RA–; c) stellar surface density with data from Talbot (1980); d) star formation rate surface density normalized to the present time solar value in logarithmic scale (data taken from Lacey & Fall 1985; Güsten & Mezger 1983, filled dots –LC– and open squares –GM–, respectively); e) and f) oxygen and nitrogen abundance as $12 + \log(\text{X}/\text{H})$ with data from Shaver et al. (1983) –crosses:SH–, Fich & Silkey (1991) –stars: FS–, Fitzsimmons, Dufton & Rolleston (1992) –open triangles:FZ–, Vílchez & Esteban (1996), –open squares: VE– and Smartt & Rolleston. (1997); Smartt et al. (2001) –stars:SM.

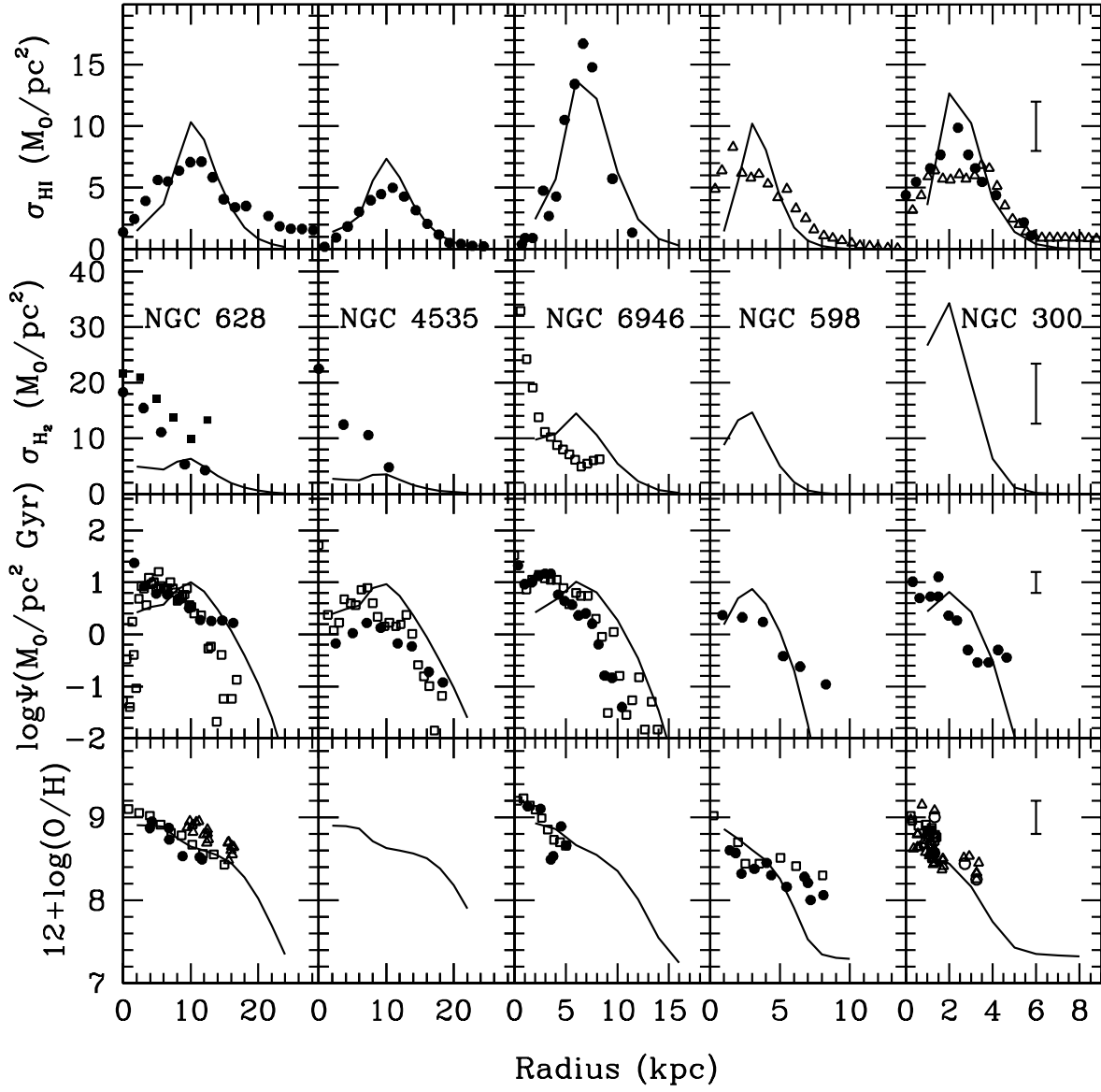


Fig. 17.— Present epoch radial distributions for atomic and molecular gas densities, (first and second rows), star formation rate (third row), and oxygen abundance $12 + \log(\text{O}/\text{H})$ (last row) for the sample used to check the grid of chemical evolution models (Table 5). The observational data are taken from references given in Table 6.

For each galaxy the distribution shows a maximum along the disk. For galaxies with similar total mass this maximum is higher for later morphological type, (NGC 4535 and NGC 6946). For galaxies of the same T, but different total mass, such as NGC 6946 and NGC 598, this maximum does not change its absolute value, but it is located at a different galactocentric distance, closer to the galaxy center for the less massive one. This shows the effect of the collapse time scale, which is longer for the less massive galaxies, thus producing a slower evolution.

We would like clear that this good fitting of data, it is essentially obtained when the most recent data and the adequate distance are used. If old worst data are taken for the comparison with models, the fit does not result good enough. In the same way the selection of the most recently obtained distances improves extraordinarily the adjustment between model and observations. This same effect is noted for all the other panels of this same Fig. 17

The radial distributions of molecular cloud surface density are shown in the second row of Fig. 17. They show a shape similar to an exponential function in the outer disk for all galaxies, but they decrease at the inner ones. We might decrease the efficiencies ϵ_H in these zones, and thus recover the exponential shape. But in this case oxygen abundances are smaller than observed in these same regions. Differences between models and data are larger than in the case of the diffuse gas, which is not unexpected, given the larger uncertainties involved in the derivation of molecular hydrogen masses. The non-dynamical treatment of the model might be the cause of these differences. However, we stress that the most recent data of molecular gas radial distributions (Nishiyama & Nakai 2001) also show a decline of the surface density for the inner disks of normal galaxies, (only barred galaxies also show, besides this hole, a strong increase of the density in the center). Our models reproduce this characteristic even if dynamical effects are not taken into account.

The radial distribution of the star formation rate for each galaxy is shown in the third row of Fig 17. We see that most of the distributions show a maximum near the center, but not always in the very central region. When the galaxy has evolved rapidly, the star formation rate has decreased in the inner disk, and the maximum has moved toward the external zones. If the galaxy is of late type or its mass is small, the evolution is slower and the star formation still shows a considerable level in the central regions of the disk, producing a quasi-exponential function for the star formation rate. The absolute values in the Maximo of the star formation rate histories are higher for the most massive galaxies.

In the last row of Fig. 17, we show the oxygen abundance radial distribution for each galaxy with the corresponding observational data. The observed trend of steeper radial distributions – larger radial gradients– for the late type galaxies is reproduced by the models due to a slower collapse combined with lower efficiencies for cloud and star formation rates, which defer the creation of stars and the ejection of chemical elements to the interstellar medium. On the other hand, the strength of the spiral arm is taken into account by the radial dependence of parameter μ which is larger for the inner regions of the disks. The star formation rate results higher in the inner disk,

thus producing a radial gradient of abundances.

5. Conclusions

We have run 420 models within the multiphase framework, corresponding the combination of to 42 different mass radial distributions and 10 evolutionary rates, corresponding to 10 efficiency values for the molecular cloud and spontaneous star formation processes, respectively.

The results obtained in this bi-parametric grid may be compared with any galaxy of given total mass (or equivalently, maximum rotation velocity) and morphological type. These results include for each radial region of halo and disk, the total mass included in the region, the star formation rate, the mass in each phase, diffuse and molecular gas, low and high mass stars, remnants, (types I and II supernova rates, and abundances for 15 elements.

The models reproduce adequately most of the global characteristics observed in spiral galaxies along the Hubble Sequence. In fact, taking into account that, with the exception of the calibration done with the Milky Way galaxy (MWG), the grid has not been computed to compare with specific galaxies, the performed comparison between model results with data must be considered very good. Actually, to our knowledge, there are not other chemical evolution models which compare predicted with observed radial distributions of diffuse and molecular gas, star formation rate and abundances for disk galaxies other than MWG. In this sense our models should be considered as an improvement over the standard ones.

1. The atomic gas shows a maximum in its radial distribution for all galaxies. This maximum is nearer to the center in the late and less evolved galaxies than in the more massive galaxies, for which the maximum is along the disk and moving toward the outer zones. This behavior produces, in some cases, a *hole* in the central zone for the diffuse gas
2. The molecular gas evolves with a time delay with respect to that of the atomic gas. Thus, the maximum of this distribution lasts longer in the center than in the case of the diffuse gas. A central maximum and an exponential function for the molecular gas are found as usually observed.
3. The H_2/M_{gas} ratio increases from the late to early type galaxies as the efficiency of the formation of molecular clouds also increases. However, models seem to indicate that the earliest and most massive galaxies have already consumed some of this molecular gas, showing a decrease in the ratio on the disk, in comparison with intermediate type galaxies.
4. The oxygen abundance reaches a maximum level, as a consequence of an saturation effect which occurs earlier for the massive and early type galaxies. The less evolved galaxies do not reach this saturation level, except in the central region, and therefore show a steep radial gradient. This correlation is in agreement with data (Vila-Costas & Edmunds 1992; Zaritsky,

Kennicutt & Huchra 1994; Garnett et al. 1997). The effect of this saturation in the oxygen abundance has also been recently observed in the inner regions of the Galaxy (Smartt et al. 2001).

5. The less massive and latest type galaxies have not yet developed a radial gradient of oxygen abundances, and show flat radial distributions. This simulates an effect on-off: for $T = 7$ a radial gradient appears if $\lambda > 0.15$ while at $T = 8$ it only appears for $\lambda \sim 1.50$. This behavior is in agreement with observations and solves the apparent inconsistency shown by trends giving steep gradients for late type galaxies and flatter ones for the earliest ones, while, at the same time most irregulars show no gradient at all and very uniform abundances.

The time evolution of these models as well as the spectrophotometric evolution are obvious steps forward in this kind of works and will be carry out in the near future.

We thank the anonymous referee for the large number of useful suggestions. This work has been partially funded by the Spanish Ministerio de Ciencia y Tecnología through the project AYA-2000-093, Italian MURST and NATO Collaborative Linkage Grant PST.CLG.976036. This work has made use of the Nasa Astrophysics Data System, and the NASA/IPAC Extragalactic Database (NED), which is operated by the Jet Propulsion Laboratory, Caltech, under contract with the National Aeronautics and Space Administration.

REFERENCES

- Abia, C. & Rebolo, R. 1989, *ApJ*, 347, 186
- Adler, D. S. & Liszt, H. S. 1989, *ApJ*, 339, 836.
- Barbuy, B. & Erdelyi-Mendes, M. 1989, *A&A*, 214, 239
- Barry, D. C. 1988, *ApJ*, 334, 436
- Belley, J. & Roy, J. 1992, *ApJS*, 78, 61.
- Boesgaard, A. M., King, J. R., Deliyannis, C. P., & Vogt, S. S. 1999, *AJ*, 117, 492
- Boissier, S. & Prantzos, N. 2000, *MNRAS*, 312, 398
- Braun, J. M. 2001, Dwarf Galaxies and their Environment, Proceedings of the Bonn/Bochum-Graduiertenkolleg International Conference, Germany, 23-27 January 2001, Eds.: de Boer K.S., Dettmar R.-J., Klein U., Shaker Verlag, p. 5
- Bronfman, L., Cohen, R. S., Alvarez, H., et al. 1988, *ApJ*, 324, 248
- Bronfman, L., Casassus, S., May, J., & Nyman, L.-Å. 2000, *A&A*, 358, 521

- Carignan, C., Charbonneau, P., Boulanger, F., & Viallefond, F. 1990, *A&A*, 234, 43
- Carlbergh, R. G., Dawson, P. C., Hsu, T. et al. 1985, *ApJ*, 294, 674
- Castellanos, M., Díaz, A. I., & Terlevich, E. 2002, *MNRAS*, 329, 315
- Cayatte, V., van Gorkom, J. H., Balkowski, C., & Kotanyi, C. 1990, *AJ*, 100, 604
- Chang, R.X, Hou, J.L., Shu, C.G., & C.Q. Fu 1999, *A&A*, 350, 38
- Christensen, T., Petersen, L., & Gammelgaard, P. 1997, *A&A*, 322, 41.
- Clayton, D. D. 1987, *ApJ*, 315, 451
- Clayton, D. D. 1988, *MNRAS*, 234, 1
- Corbelli, E. & Salucci, P. 2000, *MNRAS*, 311, 441.
- Deharveng, L., Caplan, J., Lequeux, J., Azzopardi, M., Breysacher, J., Tarengi, M., & Westerlund, B. 1988, *A&AS*, 73, 407
- de Blok, W. J. G. & McGaugh, S. S. 1996, *ApJ*, 469, L89
- Díaz, A. I., & Tosi, M. 1984, *MNRAS*, 208, 365
- Díaz, A. I., Castellanos, M., Terlevich, E., & García-Vargas, M. L. ;. 2000 *MNRAS*, 318, 462
- Dutil, I., & Roy, J.-R. 1999, *ApJ*, 516, 62
- Edvardsson, B., Andersen, J., Gustafsson, B., Lambert, D. L., Nissen, P. E., & Tomkin, J. 1993, *A&A*, 275, 101
- Ferguson, A. M. N., Gallagher, J. S., & Wyse, R. F. G. 1998, *AJ*, 116, 673
- Ferrini, F. & Galli, D. 1988, *A&A*, 195, 27
- Ferrini, F., Matteucci, F., Pardi, C., & Penco, U. 1992, *ApJ*, 387, 138
- Ferrini, F., Mollá, M., Pardi, C., & Díaz, A. I. 1994, *ApJ*, 427, 745
- Ferrini, F., Palla F., & Penco, U. 1990, *A&A*, 213, 3
- Fich, M. & Silkey, M., 1991, *ApJ*, 366, 107
- Firmani, C. & Avila-Reese, V. 2000, *MNRAS*, 315, 457
- Fitzsimmons, A., Dufton, P.L. & Rolleston, W.R.J. 1992, *MNRAS*, 259, 489
- Gallagher, J. S., Hunter, D. A., & Tutukov, A. V. 1984, *ApJ*, 284, 544

- Galli, D. & Ferrini, F. 1988, *A&A*, 218, 31
- Garnett, D. R., Shields, G. A., Skillman, E. D., Sagan, S. P., & Dufour, R. J. 1997, *ApJ*, 489, 63
- Garwood, R.W. & Dickey, J.M. 1989, *ApJ*, 338, 41
- Götz, M., & Köppen, J. 1992, *A&A*, 262, 455
- Grabelsky, D.A., Cohen, R.S. & Bronfmann, L. 1987, *ApJ*, 315, 122
- Graham, A.W. & de Block, W.J.G. 2001, *ApJ*, 556, 177
- Gratton, R. G., Sneden, C., Carretta, E., & Bragaglia, A. 2000, *A&A*, 354, 169.
- Grevesse, N., Sauval, A.J., 1998, in: *Solar composition and its evolution – from core to corona*,
Eds. Fronlich G., Huber M.C.E., Solanki S.K., von Steiger R. (Kluwer, Space Sciences Series
of ISSI, vol. 5), 161
- Güsten, R. & Mezger, P.G. 1983, *Vistas in Astronomy*, 26, 159
- Guzmán, R., Koo, D. C., Faber, S.M., et al. 1996, *ApJ* 460, L5
- Hausman, M. A. & Roberts, W. W. 1984, *ApJ*, 282, 106
- Henry, R. C. B. & Worthey, G. 1999, *PASP*, 111, 919
- Hou, J. L., Prantzos, N. & Boissier, S. 2000, *A&A*, 362, 921
- Iwamoto, K., Brachwiz, F., Nomoto, K. et al. 1999, *ApJSS*, 125, 439
- Karachentsev, I. D., Sharina, M. E., & Huchtmeier, W. K. 2000, *A&A*, 362, 544.
- Kennicutt, R. C., Jr. 1989, *ApJ*, 344, 685
- Kennicutt, R. C., Jr. & Garnett, D.R. 1996, *ApJ*, 456, 518
- Kenney, J. D., & Young, J. S. 1989, *ApJ*, 344, 171
- Kim, M., Kim, E., Lee, M. G., Sarajedini, A., & Geisler, D. 2002, *AJ*, 123, 244.
- Klessen, R. S. 2001, *ApJ*, 556, 837
- Koda, J., Sofue, Y., Wada, K. 2000, *ApJ*, 532, 214
- Köppen, J. 1994, *A&A*, 281, 26
- Kroupa, P. 2001, *MNRAS*, 322, 231
- Kwitter, K. B. & Aller, L. H. 1981, *MNRAS*, 195, 939.

- Lacey, C. G. & Fall, S. M. 1985, *ApJ*, 290, 154
- Lada, C. L. , Margulis, M., Sofue, Y., et al. 1988, *ApJ*, 328, 143
- Lelièvre, M. & Roy, J. ; 2000, *AJ*, 120, 1306
- Legrand, F. 2000, *A&A*, 354, 504
- Lynden-Bell, D. 1975, *Vistas in Astronomy*, 19, 299
- Martin, C. L. & Kennicutt, R. C. 2001, *ApJ*, 555, 301.
- McCall, M. L., Rybsky, P. M., & Shields, G. A. 1985, *ApJS*, 57, 1
- Meléndez, J., Barbuy, B., & Spite, F. ;. 2001, *ApJ*, 556, 858.
- Meyer, M. R., Adams, F. C., Hillebrandt, L. A., Carpenter, J. M., & Larson, R. B. 2000, in *Protostars & Planets IV*, Eds. Manning, V., Boss, A. P., & Russell, S. S.(Tucson: the University of Arizona Press), p.121
- Mirabel, I. F. 1989, *IAU Colloq. 120: Structure and Dynamics of the Interstellar Medium*, 396
- Mollá, M., Ferrini, F., 1995, *ApJ*, 454,726
- Mollá, M., Ferrini, F., & Díaz, A. I. 1996, *ApJ*, 466, 668
- Mollá, M., Hardy, E., & Beauchamp, D. 1999, *ApJ*, 513, 695
- Mollá, M., Ferrini, F., & Gozzi, G. 2000, *MNRAS*, 316, 345.
- Mollá, M., & Roy, J.-R., 1999, in *Chemical Evolution from zero to high redshift*, Eds. J.R. Walsh & M. R. Rosa (Springer-Verlag: Berlín), 155
- Natali, G., Pedichini, F., & Righini, M. 1992, *A&A*, 256, 79.
- Nishiyama, K. & Nakai, N. 2001, *PASJ*, 53, 713
- Nomoto, K., Thielemann, F. K., & Yokoi, K. 1984, *ApJ*, 286, 644
- Oey, M. S., & Kennicutt, R. C. 1993, *ApJ*, 411, 137
- Pagel, B. E. J. & Patchett, B. E. 1975, *MNRAS*, 172, 13
- Pagel, B. E. J., Edmunds, M. G., Blackwell, D. E., Chun, M. S., & Smith, G. 1979, *MNRAS*, 189, 95.
- Pagel, B. E. J. 1990 in *Nuclei in the Cosmos* ed. H. Oberhummer(Berlin Heidelberg: Springer-Verlag), p. 97
- Pagel, B. E. J. & Tautvaisiene, G. 1998, *MNRAS*, 299, 535

- Palunas, P. & Williams, T.B. 2000, AJ, 120, 2884
- Pardi, M. C., Ferrini, F. & Matteucci, F. 1995, ApJ, 444, 207
- Parravano, A. 1989, ApJ, 347, 812
- Peimbert, M. 1979, in I.A.U. Symp. 84, *The Large Scale Characteristics of the Galaxy*, Ed. W. B. Burton, (Reidel: Dordrecht), p.307
- Peimbert, M. & Serrano, A. 1982, MNRAS, 198, 563
- Persic, M., Salucci, P. & Steel, F. 1996, MNRAS, 281, 27, (PSS)
- Pilyugin, L. S. 2001, A&A, 369, 594
- Pilyugin, L. S. 2000, A&A, 362, 325
- Portinari, L. & Chiosi, C. 1999, A&A, 350,
- Puche, D., Carignan, C., & Bosma, A. 1990, AJ, 100, 1468.
- Rana, N. C. 1991, ARAA, 29, 129
- Renzini, A., & Voli, M. 1981, A&A, 94, 175
- Roberts, W. W. & Hausman, M. A. 1984, ApJ, 277, 744
- Rocha-Pinto, H. J., Scalo, J., Maciel, W. J., & Flynn, C. 2000, A&A, 358, 869.
- Rocha-Pinto, H. J., Maciel, W. J., Scalo, J., & Flynn, C. 2000, A&A, 358, 850.
- Rocha-Pinto, H. J. & Maciel, W. J. 1996, Rev.Mex.Astr. 2, 130
- Rogstad, D. H., Chu, K., & Crutcher, R. M. 1979, ApJ, 229, 509
- Ryder, S. D. 1995, ApJ, 444, 610
- Sage, L. J. & Solomon, P. M. 1989, ApJ, 342, L15.
- Samland, M., Hensler, G. & Theis, Ch. 1997, ApJ, 476, 544
- Sancisi, R., Fraternali, F., Oosterloo, T., van Moorsel, G. 2001, ASP. Conf. Series, Vo. 230, 111
Eds. J.E. Hibbard, M.P. Rupen and J.H. van Gorkom
- Sabdage, A, 1987, AJ, 93, 610
- Scalo, J. M. 1986, Fundamentals of Cosmic Physics, 11, 1.
- Scalo, J. 1998, ASP Conf. Ser. 142: The Stellar Initial Mass Function (38th Herstmonceux Conference), Eds. Gilmore, G. & Howell, D. (San Francisco: ASP), 201.

- Schuster, W. J. & Nissen, P. E. 1989, *A&A*, 222, 69
- Sellwood, J. A. & Kosowsky, A. 2001, *ASP. Conf. Series*, Vo. 230, ,Eds.J.E.Hibbard, M.P. Rupen and J.H. van Gorkom
- Shaver, P. A., McGee, R. X., Newton, L. M., et al. 1983, *MNRAS*, 204, 53
- Smartt, S. J., Venn, K. A., Dufton, P. L., Lennon, D. J., Rolleston, W. R. J., & Keenan, F. P. 2001, *A&A* 367, 86
- Smartt, S. J. & Rolleston, W. R. J. 1997, *ApJ*, 481, L47
- Sommer-Larsen, J. & Yoshii, Y. 1989, *MNRAS*, 238, 133
- Tacconi, L. J. & Young, J. S. 1986, *ApJ*, 308, 600.
- Talbot, R. J. 1980, *ApJ*, 235, 821
- Tinsley, B.M 1980, *Fund. Cosmic. Phys.*, 5, 287
- Tosi, M., & Díaz, A. I. 1985, *MNRAS*, 217, 571
- Tosi, M. & DDíaz, A. I. 1990, *MNRAS*, 246, 616
- Tully, R.B. 1988, *Nearby Galaxies Catalog*, Cambridge University Press,Cambridge
- Twarog, B. A. 1980, *ApJ*, 242, 242
- Simien, F. & de Vaucouleurs, G. 1986, *ApJ*, 302, 564
- van den Hoek, L. B., de Blok, W. J. G., van der Hulst, J. M., & de Jong, T. 2000, *A&A*, 357, 397
- van Zee, L., Salzer, J. J., Haynes, M. P., O'Donoghue, A. A., & Balonek, T. J. 1998, *AJ*, 116, 2805.
- Verter, F. & Hodge, P. 1995, *ApJ*, 446, 616
- Vila-Costas, B., & Edmunds, M. G. 1992, *MNRAS*, 259, 121
- Vilchez, J. M., Pagel, B. E. J., Díaz, A. I., Terlevich, E., & Edmunds, M. G. 1988, *MNRAS*, 235, 633.
- Vílchez, J. M. & Esteban, C. 1996, *MNRAS*, 280, 720
- Walsh, J.R., & Roy J.-R. 1997, *MNRAS*, 288, 726
- Wevers, B. M. H. R., van der Kruit, P. C., & Allen, R. J. 1986, *A&AS*, 66, 505.
- Wilson, C. D., Scoville, N. et al. 1988, *ApJ*, 333, 611
- Wilson, C. D. 1995, *ApJ*, 448, L97

Wyse, R. F. G. 1997, ApJ, 490, L69

Woosley, S. E. & Weaver, T. A. 1986, IAU Colloq. 89: Radiation Hydrodynamics in Stars and Compact Objects, 91

Woosley, S. E. & Weaver, T. A. 1995, ApJS, 101, 181

Wouterlook, J.G.A., Brand, J., Burton, W.B. & Kwee, K. K. 1990 A&A, 230, 21

Zaritsky, D., Kennicutt, R. C., & Huchra, J. P. 1994, ApJ, 420, 87

Table 6. Galaxy Sample Data References.

Galaxy	D	HI	H ₂	SFR	[O/H]
NGC 300	21	17,18	...	7	3,7, 16
NGC 598	11	5	...	10	12,23
NGC 628	13	24	1,19	13,15	2,14,22
NGC 4535	21	6	9	10,13	...
NGC 6946	8	4	17	10,13	2,14

(1)Adler & Liszt (1989); (2)Belley & Roy (1992); (3)Christensen, Petersen, & Gammelgaard (1997); (4)Carignan et al. (1990); (5)Corbelli & Salucci (2000); (6)Cayatte et al. (1990); (7)Deharveng et al. (1988); (8)Karachentsev, Sharina, & Huchtmeier (2000); (9)Kenney & Young (1989); (10)Kennicutt (1989); (11)Kim et al. (2002); (12)Kwitter & Aller (1981); (13)Martin & Kennicutt (2001); (14)McCall, Rybsky & Shields (1985);(15)Natali, Pedichini, & Righini (1992); (16)Pagel et al. (1979); (17)Puche, Carignan, & Bosma (1990); (18)Rogstad, Chu, & Crutcher (1979); (19)Sage & Solomon (1989); (20)Tacconi & Young (1986); (21)Tully (1988); (22)van Zee, Salzer & Haynes (1998); (23)Vilchez et al. (1988); (24)Wevers, van der Kruit, & Allen (1986)